

MOX-Report No. 109/2024

**A PCA and mesh adaptation-based format for high compression of
Earth Observation optical data with applications in agriculture**

Liverotti, L.; Ferro, N.; Matteucci, M.; Perotto, S.

MOX, Dipartimento di Matematica
Politecnico di Milano, Via Bonardi 9 - 20133 Milano (Italy)

mox-dmat@polimi.it

<https://mox.polimi.it>

A PCA and mesh adaptation-based format for high compression of Earth Observation optical data with applications in agriculture

Luca Liverotti¹, Nicola Ferro¹, Matteo Matteucci², Simona Perotto¹

December 27, 2024

¹ MOX-Department of Mathematics, Politecnico di Milano, Piazza Leonardo da Vinci 32, Milan, 20133, MI, Italy; {luca.liverotti, nicola.ferro, simona.perotto}@polimi.it

² Department of Electronics, Information and Bioengineering, Politecnico di Milano, Piazza Leonardo da Vinci 32, Milan, 20133, MI, Italy; matteo.matteucci@polimi.it

Abstract

Earth Observation optical data are critical for agriculture, supporting tasks like vegetation health monitoring, crop classification, and land use analysis. However, the large size of multispectral and hyperspectral datasets poses challenges for storage, transmission, and processing, particularly in precision farming and resource-limited contexts. This work presents the H²-PCA-AT (Hilbert and Huffman-encoded Principal Component Analysis-Adaptive Triangular) format, a novel lossy compression framework that combines PCA for spectral reduction with anisotropic mesh adaptation for spatial compression. Adaptive triangular meshes capture image features with fewer elements with respect to a standard pixel grid, while efficient encoding with Hilbert curves and Huffman coding ensures compact storage. Numerical evaluations on data reconstruction, vegetation index computation, and land cover classification demonstrate the H²-PCA-AT format effectiveness, achieving superior compression compared to JPEG while preserving essential agricultural insights.

Keywords: Earth observation, Optical satellite data, Precision Agriculture, Principal Component Analysis, Anisotropic Mesh Adaptation, Support Vector Machine, Finite Elements

1 Introduction

Earth Observation (EO) data play a pivotal role in advancing environmental monitoring related to sustainability [1, 2, 3], particularly in agriculture [4, 5].

Optical satellite data have become indispensable tools for monitoring vegetation health, classifying crop types, and assessing land use through indices like the Normalized Difference Vegetation Index (NDVI). These applications support precision farming and resource optimization, enabling sustainable practices that enhance productivity while minimizing environmental impact. For instance, monitoring crop growth phases or detecting early signs of stress caused by pests or droughts helps farmers take timely and targeted actions. The utility of EO data has been extensively demonstrated by global EO programmes such as Landsat [6] in the United States, ResourceSat [7] in India, and Gaofen [8] in China, which offer critical insights into environmental and agricultural phenomena. In the European context, the EO programme Copernicus [9] with Sentinel satellite constellations provide open-access data that are widely used for several applications in agriculture, forestry, and emergency management [1, 2, 4, 5].

Among the data sources available, Synthetic Aperture Radar (SAR) data excels in capturing structural and geometric details irrespective of weather or lighting conditions [10]. This complements optical imagery [11, 12], which is particularly significant, as it captures the chemical and physical characteristics of the Earth's surface. Specifically, optical data, acquired in multispectral and hyperspectral bands [13], offer a detailed view of vegetation health, soil conditions, and water properties. Multispectral data provide broad spectral coverage, while hyperspectral imagery enhances detail by recording hundreds of narrow spectral bands, allowing for advanced analyses such as material identification and vegetation stress detection. These properties make optical imagery indispensable in agriculture.

The sheer size of modern EO datasets—often tens of gigabytes or even terabytes per image due to increasing spatial, spectral, and temporal resolutions—poses significant challenges for storage, transmission, and processing. Optical images, in particular, consist of millions of pixels per band across dozens or hundreds of spectral bands, creating substantial bottlenecks for applications. These challenges are especially acute in precision farming, where timely access to data is crucial for informed decision-making at the field level, and in contexts with limited computational and storage resources, such as developing regions or small-scale agricultural operations. Efficient compression methods are therefore essential to enable broader and more practical use of EO data in agriculture and related fields. Compression algorithms for EO data fall into two main categories: lossless and lossy methods [14, 15, 16]. Lossless compression preserves every detail of the original data, making it ideal for scientific studies where accuracy is paramount. However, the reduction in data size is modest, often insufficient for practical purposes. In contrast, lossy compression allows for much higher compression by discarding less critical information, making it more suitable for applications like agriculture, where qualitative insights are often more valuable than pixel-level precision.

Mathematical approaches have been extensively employed to tackle the challenges of EO data compression. Principal Component Analysis (PCA) is a prominent technique for dimensionality reduction, extracting the most significant features from high-dimensional data while minimizing information loss [17]. This has made PCA a popular choice for compressing optical datasets, where it reduces the number of spectral bands required for effective analysis [18, 19, 20, 21, 22].

In this paper, we propose an innovative PCA-based lossy compression method, specifically tailored to large EO multiband optical datasets with a particular interest agricultural applications. The approach combines PCA for spectral dimensionality reduction with anisotropic mesh adaptation [23, 24] for spatial compression. The key insight is to represent optical images on adaptive triangular meshes that closely follow the variations in image features, thus replacing standard uniform pixel grids. This enables a drastic reduction in data size, while retaining sufficient detail for agricultural decision-making [25, 26]. The proposed process performs a two-level compression followed by an efficient encoding and storage procedure. First, the spectral data are compressed through PCA and projected onto a lower-dimensional space, while preserving the most informative features. Successively, a further compression is carried out by constructing a triangular tessellation of the image, with tiles concentrated in regions of high feature variation, such as field boundaries or vegetation gradients. This results in a representation that uses far fewer elements than the original pixel grid. Finally, the triangular mesh is encoded using Hilbert curves [27] for spatial indexing and Huffman coding [28] for compact representation, minimizing storage requirements. We will refer to the outcome of this compression process as to H^2 -PCA-AT (Hilbert and Huffmann-encoded PCA-Adaptive Triangular) format. This new format becomes effective in practice through a decoding phase – based on a modified Delaunay algorithm – that recovers the original optical observation.

The contribution of this work is twofold: first, it demonstrates the effectiveness of combining PCA, anisotropic mesh adaptation and efficient encoding algorithms for EO data compression; second, it validates the H^2 -PCA-AT format when involved in applications that are directly relevant to agriculture. Specifically, the new format is tested for reconstruction of optical data, NDVI computation, and land cover classification. Comparisons with standard JPEG compression [29] highlight the superior performance of our approach in preserving information critical for these tasks.

The paper is organized as follows. Section 2 introduces the AT representation for single-band images, highlighting the foundational principles. Section 3 extends this approach to multiband optical data by sequentially combining the encoding phase, relying on PCA and AT compression, Hilbert and Huffman algorithms, with the decoding step. Numerical assessments for data reconstruction, NDVI computation, and land cover classification are

presented in Section 4. Finally, Section 5 discusses the pros and cons of the H²-PCA-AT format and outlines potential future developments.

2 Adaptive Triangular representation of an image

Image representation refers to the method of converting a picture into a digital format that can be processed by a computational system. There is a wide range of image representation methods proposed in the past few decades, with associated pros and cons [30]. In this paper, we refer to raster images, which are commonly used for digital photographs, computer graphics, and other types of complex images. A raster image consists of a regular grid of square cells – called pixels (px) – with an associated numerical value representing the brightness at a specific location of the object depicted in the image.

From a mathematical point of view, an image I of dimensions m and n can be encoded as a discontinuous function $v_I : [0, m] \times [0, n] \rightarrow \mathbb{R}$, such that

$$v_I(x_j, y_i) = I_{i,j} \quad \text{for } x_j \in [j - 1, j], y_i \in [n - i, n - (i - 1)], \quad (1)$$

where $I_{i,j}$ denotes the value of the image at the pixel (i, j) , with $i = 1, \dots, n$, $j = 1, \dots, m$. The uniform structure inherent in a raster image (i.e., the equal size of pixels) may encounter certain limitations:

- superfluous pixels may be used to represent areas with few details, resulting in redundant information being stored;
- not enough pixels may be employed to represent highly detailed areas.

These considerations prompted the idea of replacing the uniform pixel grid underlying the raster format with an alternative tessellation adapted to the image details, where large and small tiles are displaced in correspondence with low- and high-detailed areas, respectively. For instance, in [31] the authors resort to an image representation based on different resolution levels, relying on a quadtree decomposition procedure. In [32], the utilization of a non-uniform grid of triangular cells is employed in an image segmentation framework, demonstrating the high flexibility of simplicial elements in tracing curvilinear contours, when compared with squares.

In this work, we introduce an automatic and handy procedure for a triangular adaptive image representation that eliminates the tedious parameter tuning required in [32], by generalizing the approach in [33] used for image segmentation. Throughout the paper, we categorize the proposed image representation method as Adaptive Triangular (AT). In particular, we distinguish between an isotropic and an anisotropic AT representation. An isotropic one comprises primarily equilateral triangles, whereas an

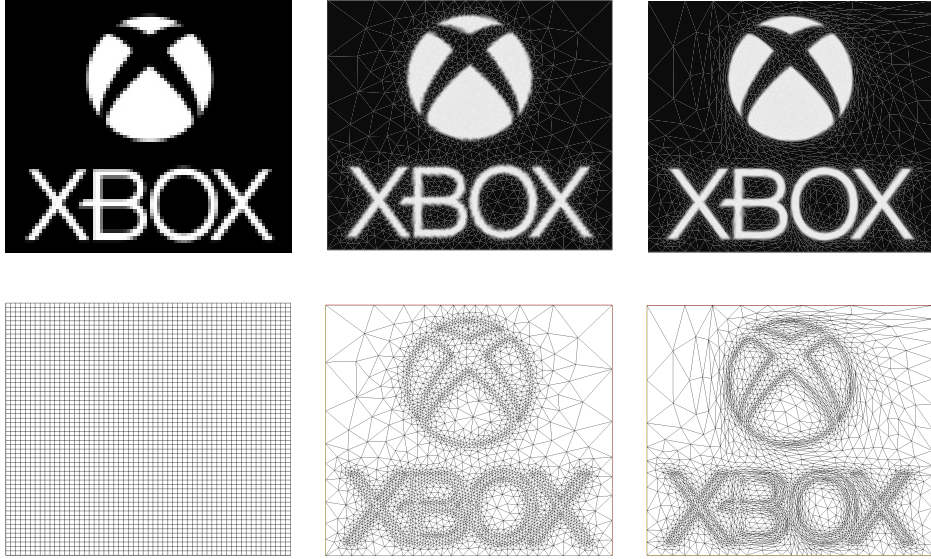


Figure 1: Comparison among the representation of an image (top) associated with different tessellations (bottom): standard pixel-wise grid – 6375 tiles (left); isotropic AT representation – 6360 tiles (center); anisotropic AT representation – 6372 tiles (right).

anisotropic AT representation may also include highly stretched triangular tiles.

Figure 1 highlights the advantages of using triangular tiles, by comparing the visualization of a benchmark image on a standard pixel-wise tessellation (left column) with an isotropic (center column) and an anisotropic (right column) AT representation, when using about the same number of tiles. From a qualitative perspective, both AT representations outperform the pixel-wise description of the image. Indeed, the appropriately sized (center and right), shaped, and oriented (right) triangular tiles enable the sharp description of both the logo and the text contours. In the following sections, we focus on the anisotropic AT tiling since it effectively eliminates the jagged boundaries that are still present in the isotropic AT representation. This ensures the desirable balance between image accuracy and storage space.

2.1 Constructing the anisotropic AT representation

AT representations rely on a well-consolidated mathematical tool for the numerical approximation of a partial differential equation (PDE), for instance, in a finite element (FE) setting. In fact, the tessellations discussed in the previous section mirror the computational meshes discretizing the domain of a differential problem. For instance, with reference to Figure 1, the pixel-wise

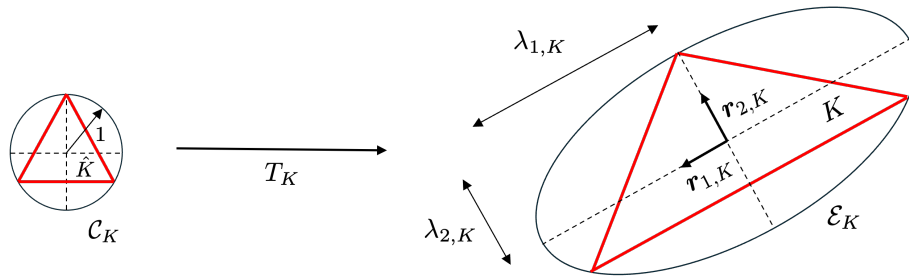


Figure 2: Sketch of the affine map T_K and associated anisotropic quantities.

grid in the left column corresponds to a structured square mesh, whereas the isotropic and anisotropic AT representations do coincide with an unstructured isotropic and anisotropic adapted triangular mesh, respectively. This correspondence between an image tessellation and a computational mesh leads us to employ well-established techniques for mesh adaptation in the context of an AT representation, with a particular focus on an anisotropic setting.

To generate an adapted mesh it is common practice to resort to a mathematical tool, such as an a priori/a posteriori error estimator, to identify the regions requiring mesh modifications. Alongside this, an adaptive procedure is employed to adjust the grid based on this information. The error estimation and the adaptive mesh generation procedures are detailed in the following subsections.

2.1.1 Error estimation: the theoretical backbone

The procedure of mesh adaption we employ is based on the approach outlined in [24], which exploits an anisotropic a posteriori error estimator. As an initial step, we select the source of information used to identify the anisotropic characteristics of mesh elements. With reference to Figure 2, we refer to the anisotropic framework proposed in [23]. Here, the size, shape, and orientation of the generic element K of a mesh \mathcal{T}_h are recovered from the spectral properties of the affine map $T_K : \hat{K} \rightarrow K$, which changes the reference triangle \hat{K} into K (and analogously the circle \mathcal{C}_K into the ellipse \mathcal{E}_K). The anisotropic features of element K are fully characterized by the directions, $\mathbf{r}_{i,K}$, and the lengths, $\lambda_{i,K}$, of the semi-axes of \mathcal{E}_K , with $i = 1, 2$, after assuming $\lambda_{1,K} \geq \lambda_{2,K}$.

It is customary to measure the anisotropy of the element K through the aspect ratio $s_K = \lambda_{1,K}/\lambda_{2,K} \geq 1$, where equality $s_K = 1$ corresponds to the isotropic case.

Concerning the function framework used to contextualize the a posteriori analysis, we refer to the standard spaces $C^0(\bar{\Omega})$, $L^2(\Omega)$ and $H^1(\Omega)$ associated with a generic domain $\Omega \subset \mathbb{R}^2$, and we introduce the FE spaces of piecewise

constant and linear polynomials [34]

$$\begin{aligned} V_h^0(\mathcal{T}_h) &= \left\{ v \in L^2(\Omega) : v|_K \in \mathbb{P}^0(K), \forall K \in \mathcal{T}_h \right\}, \\ V_h^1(\mathcal{T}_h) &= \left\{ v \in C^0(\overline{\Omega}) : v|_K \in \mathbb{P}^1(K), \forall K \in \mathcal{T}_h \right\}, \end{aligned}$$

associated with a tessellation \mathcal{T}_h of Ω , with $\mathbb{P}^m(K)$ the set of polynomials of degree $m = 0, 1$, defined on K . Functions v_h in V_h^m are univocally identified by the so-called degrees of freedom, $\text{DOF}[v_h]$, coinciding with the values taken by v_h at the barycenter and at the vertices of the triangles for $m = 0$ and $m = 1$, respectively.

Now, we select the error estimator. With reference to the available literature on a posteriori error analyses [35, 36, 37], we opt for a recovery-based error estimator, in line with the approach by O.C. Zienkiewicz and J.Z. Zhu [38]. In this context, the authors estimate the $H^1(\Omega)$ -seminorm of the discretization error linked to the FE approximation, v_h , of the (weak) solution, v , to a PDE problem. The idea presented in [38, 39, 40] is to estimate the $H^1(\Omega)$ -seminorm of the discretization error by replacing the exact gradient, ∇v , with the so-called recovered gradient, $\nabla^R v_h$, so that

$$\begin{aligned} |v - v_h|_{H^1(\Omega)}^2 &= \sum_{K \in \mathcal{T}_h} \int_K |\nabla v - \nabla v_h|^2 dK \approx \\ &\sum_{K \in \mathcal{T}_h} \int_K |\nabla^R v_h - \nabla v_h|^2 dK = \sum_{K \in \mathcal{T}_h} \rho_K^2 = \rho^2, \end{aligned} \quad (2)$$

with ρ and ρ_K the global and local error estimators. The quantity ρ proves to be an effective tool for identifying strong gradients of v . Since anisotropic meshes further enhance a sharp detection of the solution gradient, we adopt the anisotropic variant of the estimator (2). Following [24], we pick $v_h \in V_h^1(\mathcal{T}_h)$ and we define the anisotropic counterpart of the squared error estimator ρ in (2) as

$$\eta^2 = \sum_{K \in \mathcal{T}_h} \eta_K^2 \quad \text{with} \quad \eta_K^2 = \frac{1}{\lambda_{1,K} \lambda_{2,K}} \sum_{i=1}^2 \lambda_{i,K}^2 (\mathbf{r}_{i,K}^T G_{\Delta_K}(\mathbf{E}^R) \mathbf{r}_{i,K}), \quad (3)$$

where $\mathbf{E}^R = \nabla^R v_h - \nabla v_h$ is the recovered gradient error, $G_{\Delta_K} : [L^2(\Omega)]^2 \rightarrow \mathbb{R}^{2 \times 2}$ is the symmetric semi-definite positive matrix, with entries

$$[G_{\Delta_K}(\mathbf{w})]_{rs} = \sum_{T \in \Delta_K} \int_T w_r w_s dT \quad r, s = 1, 2,$$

for any vector-valued function $\mathbf{w} = [w_1, w_2]^T \in [L^2(\Omega)]^2$, and $\Delta_K = \{T \in \mathcal{T}_h : T \cap K \neq \emptyset\}$ is the patch of elements associated with K . According to [24], we select the area-weighted average of the discrete gradient over Δ_K as recovered gradient, namely

$$\nabla^R v_h|_K(\mathbf{x}) = \frac{1}{|\Delta_K|} \sum_{T \in \Delta_K} |T| \nabla v_h|_T(\mathbf{x}) \quad \text{for } \mathbf{x} \in K.$$

2.1.2 Mesh adaptation: a practical procedure

The information provided by the anisotropic estimator η is exploited to update the computational mesh. Among the different techniques that can be adopted, we employ a metric-based approach [41] that defines the spacing of the adapted mesh through the piecewise constant symmetric positive tensor field, $M = M(\{\lambda_{i,K}, \mathbf{r}_{i,K}\}) \in \mathbb{R}^{2 \times 2}$, such that, for any $K \in \mathcal{T}_h$,

$$M \Big|_K = R_K^T \Lambda_K^{-2} R_K \quad \text{with} \quad R_K = [\mathbf{r}_{1,K}, \mathbf{r}_{2,K}]^T, \quad \Lambda_K = \text{diag}(\lambda_{1,K}, \lambda_{2,K}), \quad (4)$$

where $\lambda_{i,K}$ and $\mathbf{r}_{i,K}$ do coincide with the anisotropic quantities in Figure 2.

Following [42], we generate the adapted mesh in order to ensure a certain accuracy, τ , on the discrete solution v_h , while minimizing the mesh cardinality, $\#\mathcal{T}_h$, and equidistributing the error across the elements, i.e., $\eta_K^2 = \tau^2 / \#\mathcal{T}_h$. These requirements lead to solve an elementwise constrained minimization problem. The solution to this problem allows us to replace metric M with a new tensor $M^* = M^*(\{\lambda_{i,K}^*, \mathbf{r}_{i,K}^*\})$, employed to update \mathcal{T}_h with the adapted mesh \mathcal{T}_h^* .

In more detail, we rewrite the estimator η_K in (3) by collecting the area information as

$$\eta_K^2 = \lambda_{1,K} \lambda_{2,K} |\widehat{\Delta}_K| \left[s_K \left(\mathbf{r}_{1,K}^T \widehat{G}_{\Delta_K}(\mathbf{E}^R) \mathbf{r}_{1,K} \right) + s_K^{-1} \left(\mathbf{r}_{2,K}^T \widehat{G}_{\Delta_K}(\mathbf{E}^R) \mathbf{r}_{2,K} \right) \right], \quad (5)$$

where $\widehat{G}_{\Delta_K}(\cdot)$ is the scaled matrix $G_{\Delta_K}(\cdot) / |\Delta_K|$, $|\Delta_K| = \lambda_{1,K} \lambda_{2,K} |\widehat{\Delta}_K|$, with $\widehat{\Delta}_K = T_K^{-1}(\Delta_K)$ the pullback of the patch Δ_K through map T_K . The minimization of the mesh cardinality (or, likewise, the maximization of the element area) combined with the error equidistribution leads us to solve the constrained minimization problem

$$\min_{s_K, \mathbf{r}_{i,K}} \mathcal{J}(s_K, \mathbf{r}_{1,K}, \mathbf{r}_{2,K}) \quad \text{subject to} \quad s_K \geq 1, \quad \mathbf{r}_{i,K} \cdot \mathbf{r}_{j,K} = \delta_{i,j} \quad i, j = 1, 2,$$

with $\mathcal{J}(s_K, \mathbf{r}_{1,K}, \mathbf{r}_{2,K})$ the quantity in the square brackets in (5) and $\delta_{i,j}$ the Kronecker symbol. The solution to this problem is provided by

$$s_K^* = \sqrt{g_1/g_2}, \quad \mathbf{r}_{1,K}^* = \mathbf{g}_2, \quad \mathbf{r}_{2,K}^* = \mathbf{g}_1, \quad (6)$$

with $\{g_i, \mathbf{g}_i\}_{i=1,2}$ the eigen-pairs associated with the matrix $\widehat{G}_{\Delta_K}(\mathbf{E}^R)$. Finally, the optimal values $\lambda_{i,K}^*$ are derived by explicitly imposing the equidistribution constraint, which yields

$$\lambda_{1,K}^* = g_2^{-1/2} \left(\frac{\tau^2}{2 \#\mathcal{T}_h |\widehat{\Delta}_K|} \right)^{1/2}, \quad \lambda_{2,K}^* = g_1^{-1/2} \left(\frac{\tau^2}{2 \#\mathcal{T}_h |\widehat{\Delta}_K|} \right)^{1/2}. \quad (7)$$

The quantities $\mathbf{r}_{i,K}^*$ and $\lambda_{i,K}^*$ in (6)-(7) identify the new metric M^* (see [42] for the details). Tensor M^* represents the input for a metric-based mesh

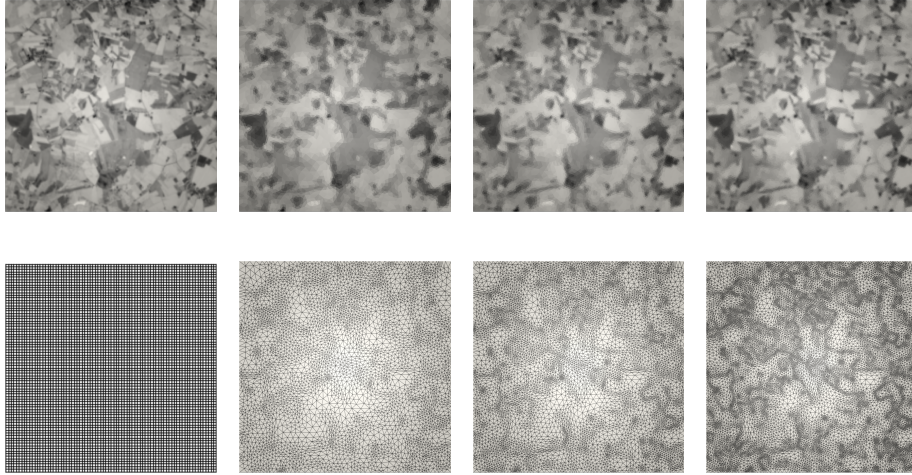


Figure 3: Portion of the SWIR-I channel of a multispectral optical satellite observation: image visualization (top) and associated tessellations (bottom) for the pixel image v_I (first column) and the AT representation for $\tau = 1.35$ (second column), $\tau = 0.90$ (third column), $\tau = 0.50$ (fourth column).

generator that returns the new adapted mesh \mathcal{T}_h^* .

For all the numerical tests of the paper, we use the grid generation environment available in the software FreeFEM [43].

2.2 The new AT representation in practice

The mesh adaptation procedure discussed in Sections 2.1.1-2.1.2 can be exploited to establish a novel image representation format aimed at efficiently managing large datasets. This is particularly relevant for optical data, which consist of multiple layered images or channels, each corresponding to a distinct range of wavelengths within the electromagnetic spectrum. As a result, these data – referred to as multispectral or hyperspectral data – often entail significant storage demands, 16 bits being, in general, allocated for the brightness value of each pixel.

As an instance of the effectiveness of the AT representation, let us consider the left panel in Figure 3 that shows a portion (400×400 px) of the SWIR-I (Short-Wave InfraRed) channel of a multispectral optical satellite observation, depicting an extensive agricultural landscape. By varying the adaptation tolerance τ in (7), we can replace the original raster image consisting of 160000 px with an anisotropic AT representation characterized by 8535 ($\tau = 1.35$), 14490 ($\tau = 0.90$), and 29607 ($\tau = 0.50$) triangular tiles. As expected, smaller values of τ yield finer meshes that exhibits a higher image reconstruction accuracy.

The three examples of AT representation in Figure 3 are yielded by particularizing the generic procedure in Sections 2.1.1-2.1.2. In particular,

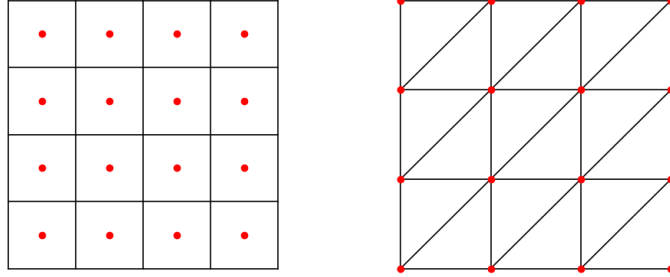


Figure 4: Construction of the initial mesh \mathcal{T}_h (right) for the AT representation, starting from a pixel grid (left). The red circles highlight the DOFs associated with the two representations.

the following choices are made:

- Ω is the rectangular image domain $(0, m) \times (0, n)$;
- mesh \mathcal{T}_h is selected as a structured triangular tessellation of Ω induced by the pixel-wise tiling of the image;
- function v in (2) coincides with v_I in (1);
- function $v_h \in V_h^1(\mathcal{T}_h)$ in (2) is identified with the piecewise linear interpolant of v_I on \mathcal{T}_h ;
- the adapted mesh \mathcal{T}_h^* is denoted by \mathcal{T}_h^v ;

The output of the AT representation of an image does coincide with the anisotropic adapted mesh, \mathcal{T}_h^v , and with the projection, \tilde{v}_h , of function v_h onto the space $V_h^1(\mathcal{T}_h^v)$.

Some comments are in order. The triangular mesh \mathcal{T}_h is generated from the square partition induced by the pixel structure of I , with the aim to preserve the number of data in the original image (see Figure 4). In particular, I contains $m \times n$ data, one value appended to each pixel barycenter, whereas space $V_h^1(\mathcal{T}_h)$ associates one value (i.e., $\text{DOF}[v_h]$) with each triangle vertex. Thus, we generate \mathcal{T}_h as a regular structured triangular mesh based on $m - 1$ and $n - 1$ uniform subintervals along the horizontal and vertical sides of Ω , respectively.

Finally, we observe that function v (i.e., v_I) does not correspond to the solution of any PDE problem, in contrast to the standard scenario discussed in Section 2.1.1. This corroborates the property of the recovery-based error estimators of being independent of the selected function v .

3 The compression method

In this section we propose a pipeline implementing a novel method for the efficient compression of multispectral and hyperspectral optical images, which exploits the effectiveness of the AT representation. As a first task, we combine the Principal Component Analysis (PCA) with the AT method to reduce the amount of data characterizing a multiband optical image, this leading to the PCA-AT representation (Section 3.1). Successively, an encoding procedure is used to efficiently store the information associated with this new representation, yielding the H²-PCA-AT format (Section 3.2). Finally, a decoding step is carried out to recover the original satellite raster data (Section 3.3).

3.1 The PCA-AT representation of a multiband optical observation

The AT representation presented in Section 2 might not always result in storage efficiency. In fact, the proposed approach is generally competitive in terms of storage of brightness values, as the number of DOFs associated with an AT representation is lower compared to the pixel count. However, a mesh information is also required to practically reconstruct the image from the DOFs vector of the finite element function associated with the AT representation. This is not the case of the standard pixel-wise format that demands only the DOFs information, the mesh being structured and allowing for direct memory access (i.e., only the image dimensions are requested). Thus, the advantage of the AT representation in terms of storage efficiency arises when the number of DOFs added to the mesh data is smaller than the DOF cardinality of a pixel-wise image. The storage issue for the AT representation becomes especially significant for multiband optical images, which consist of numerous channels, each potentially associated with a different tessellation.

The PCA-AT representation addresses this storage concern. Initially, we extract the primary features of the channels pixel-by-pixel by employing a standard PCA [17]. In particular, PCA may be employed to compress an optical observation, I_{opt} , along the channel dimension, where I_{opt} collects the brightness distribution of the c channels, $\{ch_i\}_{i=1,\dots,c}$, with $ch_i \in \mathbb{R}^{h \times w}$, h , w the dimension of each channel in terms of number of pixels. PCA reduces the cross-correlation among the channels by introducing a reduced basis $\mathcal{B} = \{b_j\}_{j=1}^k$, with $b_j \in \mathbb{R}^{h \times w}$ and $k < c$, so that each channel can be surrogated as

$$ch_i - \overline{ch_i} = \sum_{j=1}^c \alpha_i^j b_j \simeq \sum_{j=1}^k \alpha_i^j b_j \quad i = 1, \dots, c, \quad (8)$$

with $\overline{ch_i}$ the mean brightness of the i -th channel and α_i^j suitable coefficients to be determined. The greater the number k , the higher the percentage of explained data variability. In the sequel, we refer to

$$\mathbf{R}(b_j) = [b_{j,\min}, b_{j,\max}] \subset \mathbb{R}, \quad (9)$$

as to the range of values taken by the j -th basis element, with $b_{j,\min} = \min b_j$ and $b_{j,\max} = \max b_j$.

To compute the reduced basis \mathcal{B} , first we reshape the 3D array $V \in \mathbb{R}^{h \times w \times c}$, collecting the whole optical data I_{opt} , with $V[:, :, i] = ch_i, i = 1, \dots, c$, into the 2D sample-feature (with sample = pixel, feature = channel) matrix $X \in \mathbb{R}^{hw \times c}$, such that $X = \mathcal{S}_\downarrow(V)$, with $\mathcal{S}_\downarrow : \mathbb{R}^{h \times w \times c} \rightarrow \mathbb{R}^{hw \times c}$, and

$$X[(r-1)w + s, :] = V[r, q, :] \quad r = 1, \dots, h, \quad q = 1, \dots, w. \quad (10)$$

Successively, we apply the (reduced) Singular Value Decomposition (SVD) [44] to matrix $X - \overline{X}$, so that

$$X - \overline{X} = U \Sigma D^T, \quad (11)$$

with $U \in \mathbb{R}^{hw \times c}$, $D = [d_{ij}] \in \mathbb{R}^{c \times c}$ the matrices of the left and right singular vectors, $\Sigma = \text{diag}(\sigma_1, \dots, \sigma_c) \in \mathbb{R}^{c \times c}$ the matrix of the singular values. We collect the first k columns, $\{\mathbf{u}_j\}_{j=1}^k$, of U into the matrix $U_k = [\mathbf{u}_1, \dots, \mathbf{u}_k]$, with $\mathbf{u}_j \in \mathbb{R}^{hw}$. Then, we reshape U_k into the 3D volume $V_B \in \mathbb{R}^{h \times w \times k}$ such that $V_B = \mathcal{S}_\uparrow(U_k)$, with $\mathcal{S}_\uparrow : \mathbb{R}^{hw \times k} \rightarrow \mathbb{R}^{h \times w \times k}$, and

$$V_B[r, s, :] = U_k[(r-1)w + q, :] \quad r = 1, \dots, h, \quad q = 1, \dots, w. \quad (12)$$

Finally, the reduced basis \mathcal{B} is identified by

$$b_j = V_B[:, :, j] \quad j = 1, \dots, k,$$

while, from (11), coefficients α_i^j in (8) can be computed as

$$\alpha_i^j = \sigma_j d_{ij} \quad i = 1, \dots, c, \quad j = 1, \dots, k. \quad (13)$$

Figure 5, center panel, collects the first basis elements, b_1, \dots, b_4 , associated with the original multispectral observation I_{opt} in the left panel. The right panel in Fig. 5 applies the reconstruction in (8) to the input data I_{opt} .

The compression process using PCA is now smartly combined with the AT representation to minimize the amount of data to be stored. Specifically, in order to limit the mesh information, we construct the AT representation only for b_1 , and we project the basis elements b_2, \dots, b_k onto the AT tessellation $\mathcal{T}_h^{b_1}$ associated with b_1 . This choice is based on the notion that b_1 provides the most meaningful content in terms of explained variance (see Table 1), so that the associated adapted mesh is expected to adequately capture also the features of the other basis elements. In practice, the PCA-AT representation is constructed as follows:

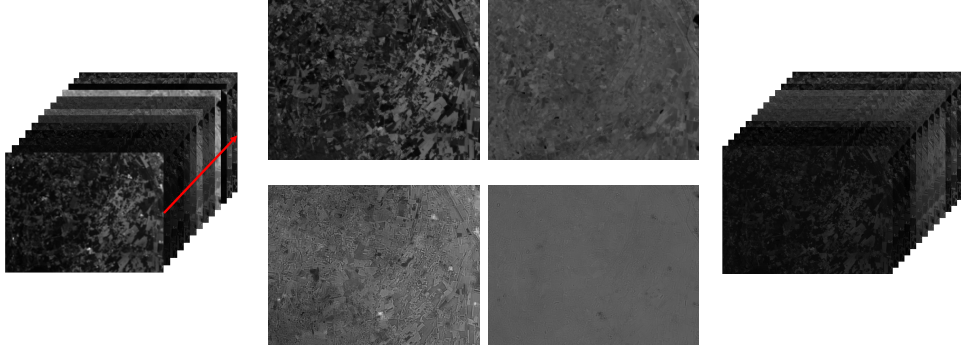


Figure 5: Instance of the PCA procedure performed along channel dimension (red arrow): channels (793×1049 px) of a Sentinel-2 optical observation covering an agricultural area (left panel); PCA basis elements b_1, \dots, b_4 (center panel, top-bottom, left-right); reconstruction of the original channels (right panel).

Table 1: Percentage of explained data variability associated with the PCA basis elements b_1, \dots, b_k corresponding to the Sentinel-2 optical data in Figure 5.

k	1	2	3	4	5	6
Explained variance [%]	61.4	88.4	94.9	97.8	98.7	99.1

- we normalize the b_1 basis domain $(0, h) \times (0, w)$ to the reference square $\mathcal{Q} = (0, 1)^2$, while maintaining the number of subdivisions along the horizontal and vertical directions [†];
- we apply the procedure in Section 2.2 to b_1 , after identifying Ω with \mathcal{Q} ; \mathcal{T}_h with the structured triangular mesh associated with the pixel-wise tessellation of b_1 ; v with b_1 ; v_h with the piecewise linear interpolant of b_1 on \mathcal{T}_h . This step delivers the AT mesh $\mathcal{T}_h^{b_1}$ along with the associated representation $\tilde{b}_1 \in V_h^1(\mathcal{T}_h^{b_1})$ of b_1 obtained by projecting b_1 onto $V_h^1(\mathcal{T}_h^{b_1})$;
- we characterize the basis elements b_j , $j = 2, \dots, k$, as functions in $V_h^1(\mathcal{T}_h)$ and we define the corresponding projections \tilde{b}_j onto the space $V_h^1(\mathcal{T}_h^{b_1})$;
- we collect functions \tilde{b}_j into the PCA-AT reduced basis $\tilde{\mathcal{B}} = \{\tilde{b}_j\}_{j=1}^k$.

[†]This choice is motivated by computational reasons, as detailed in the subsequent section. To simplify the notation, we preserve the same symbol b_1 to denote the original and the normalized basis element.

In summary, the PCA-AT representation of the optical observation I_{opt} comprises the mesh $\mathcal{T}_h^{b_1}$ and the reduced basis $\tilde{\mathcal{B}}$. This requires the storing of $[(k+2)nv]$ data – including the integer vectors $\text{DOF}[\tilde{b}_j]$ of the k basis elements and the floating point x - and y -coordinates of the nv vertices of $\mathcal{T}_h^{b_1}$ – along with the mesh connectivity. This information is mandatory when dealing with an unstructured grid and consists of triplets of integers labeling the mesh vertices according to a global numbering.

In the following we show how to eliminate mesh connectivity and how to efficiently store DOFs and vertex information, so that the PCA-AT representation becomes competitive with respect to a standard pixel-wise format (i.e., when $(k+2)nv < khw$).

3.2 H²-PCA-AT format: the encoding phase

We outline the approach for efficiently storing the information characterizing the PCA-AT representation of the optical observation I_{opt} . The proposed strategy involves encoding both the coordinates and the brightness information associated with the vertices of $\mathcal{T}_h^{b_1}$, while disregarding the mesh connectivity. This decision will prompt the development of a specialized method for reconstructing a mesh that surrogates $\mathcal{T}_h^{b_1}$ in the decoding phase.

3.2.1 Mesh vertices encoding

To encode the vertex information characterizing mesh $\mathcal{T}_h^{b_1}$, we resort to the so-called space-filling curves that allow mapping a one-dimensional set into a higher-dimensional one (e.g., an interval into a square or a cube). Space-filling curves find practical applications in several fields to optimize data storage, such as data indexing, image compression, computer graphics, geographic information systems and digital signal processing [45, 46]. Among the several options available in the literature, we adopt the Hilbert curves [27], since they are regular, ordered, and easily implementable, for instance, when compared to Peano [47] or Z-order curves [48].

With reference to a two-dimensional setting, the key idea is to iteratively divide the set $\overline{\mathcal{Q}} = [0, 1]^2$ into smaller squares and then recursively create a path – the Hilbert curve – that entirely fills $\overline{\mathcal{Q}}$ and that crosses these subdivisions, visiting a subset of points in the space exactly once. Hilbert curves feature interesting properties, such as locality preservation (close points in space tend to have nearby addresses along the curve, aiding algorithms like spatial indexing and searching) and self-similarity like fractals (the curves exhibit a similar pattern at different scales along the entire path).

The construction of a Hilbert curve is based on an iterative procedure, whose generic p -th iteration yields the level- p Hilbert curve, $C_p \subset \overline{\mathcal{Q}}$. The level p of the curve tunes the filling of $\overline{\mathcal{Q}}$ by means of C_p (see Figure 6). Formally, on varying $p \in \mathbb{N}$, with $p \geq 2$, we have $C_p = F_p(C_{p-1})$, with C_1

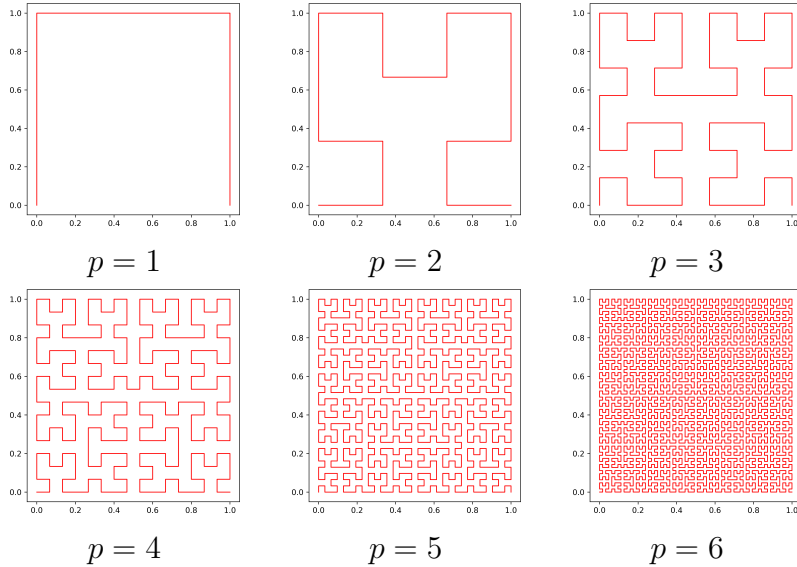


Figure 6: The level- p Hilbert curves $C_p \subset \overline{\mathcal{Q}}$, for $p = 1, \dots, 6$.

the U-curve in Figure 6 (top-left) and $F_p : \overline{\mathcal{Q}} \rightarrow \overline{\mathcal{Q}}$ a composite geometric transformation, which properly combines scaling, rotation and translation (we refer to [27] for technical details and to the Python Hilbert curve package [49] for a possible implementation). Each curve C_p is identified by the set \mathcal{H}_p of the associated breakpoints, which we refer to as Hilbert points of order p (see Figure 7). The cardinality of \mathcal{H}_p , namely $|\mathcal{H}_p|$, increases exponentially with the order p , being $|\mathcal{H}_p| = 4^p$. It is customary to introduce a one-to-one correspondence between the so-called Hilbert indices $\mathcal{I}_p = \{1, \dots, 4^p\}$ and the Hilbert points to univocally identify the elements in \mathcal{H}_p with the integer labels $1, \dots, 4^p$.

The idea underlying the proposed encoding strategy for the vertices of mesh \mathcal{T}_h^{b1} entails approximating the vertex list, $\mathcal{V} = \{V_i\}_{i=1}^{nv}$, with a subset, $\mathcal{V}_{HLB} = \{V_{HLB,i}\}_{i=1}^{nv}$, of Hilbert points of a certain order p , whose value depends on a desired accuracy τ_{HLB} . This approach leads to store the Hilbert index instead of the vertex coordinates, $(V_{i,x}, V_{i,y})$, (i.e., an integer rather than a pair of real numbers), for any vertex $V_i \in \mathcal{V}$. Taking the vertex list \mathcal{V} as input, the encoding strategy encompasses two steps:

- Identification of Hilbert order and indices – We find the Hilbert curve C_p of order p such that, for each mesh vertex V_i , there exists a Hilbert point H_i within a distance equal to the tolerance τ_{HLB} (see Figure 8). We build the array $\text{ind}_{HLB} \subset \mathcal{I}_p$ that gathers the indices of the Hilbert points H_i .
- Sorting of the Hilbert indices and final encoding – We arrange the entries of ind_{HLB} in ascending order, yielding the array $\text{ind}_{HLB, \text{sort}}$. We

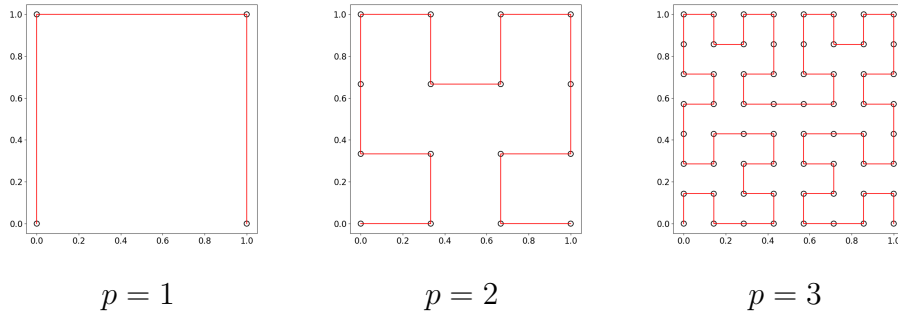


Figure 7: The level- p Hilbert curves $C_p \subset \overline{\mathcal{Q}}$ and associated Hilbert points \mathcal{H}_p , for $p = 1, \dots, 3$.

define vector \mathcal{I}_{enc} containing the first Hilbert index and the differences between two consecutive Hilbert indices.

Concerning the tolerance, τ_{HLB} can be either selected by the user or set automatically as the largest possible value ensuring the preservation of the cardinality of the original mesh $\mathcal{T}_h^{b_1}$ and avoiding vertex collapse. The replacement of the array $\text{ind}_{HLB, \text{sort}}$ with \mathcal{I}_{enc} at the second step is meant to further reduce the required memory storage, since index differences involve less digits than the integer label, especially for $|\text{ind}_{HLB, \text{sort}}| = nv \gg 1$. Finally, vertices \mathcal{V}_{HLB} coincide with the Hilbert points labeled in $\text{ind}_{HLB, \text{sort}}$, thanks to the implicit bijection between Hilbert points and indices.

3.2.2 Brightness encoding

The mesh vertices encoding requires a rearrangement of the associated brightness information. We remind that a generic finite element function $v_h \in V_h^1(\mathcal{T}_h^{b_1})$ is uniquely identified by the corresponding DOFs. In the context of multiband image compression, we denote by $\text{DOF}[\tilde{b}_j] \in \mathbb{R}^{nv}$ the vector collecting the brightness values of \tilde{b}_j at the vertices \mathcal{V} of mesh $\mathcal{T}_h^{b_1}$, with $j = 1, \dots, k$. Consequently, the vector $\text{DOF}_{HLB}[\tilde{b}_j] \in \mathbb{R}^{nv}$ gathering the brightness values of \tilde{b}_j at the vertices in \mathcal{V}_{HLB} can be assembled in a straightforward way by exploiting that \tilde{b}_j belongs to $V_h^1(\mathcal{T}_h^{b_1})$, being

$$\text{DOF}_{HLB}[\tilde{b}_j](i) = \tilde{b}_j(V_{HLB, i}) \quad i = 1, \dots, nv, \quad j = 1, \dots, k. \quad (14)$$

Typically, the brightness information is stored according to a 16-bit format. However, for store needs, we map brightness values $\text{DOF}_{HLB}[\tilde{b}_j]$ into the range $[0, 255]$, and then we apply an integer rounding, reducing the original 16-bit to an 8-bit data representation, $\text{DOF}_{HLB-8}[\tilde{b}_j]$. This procedure unavoidably leads to several repetitions in the new DOF vector. Such a

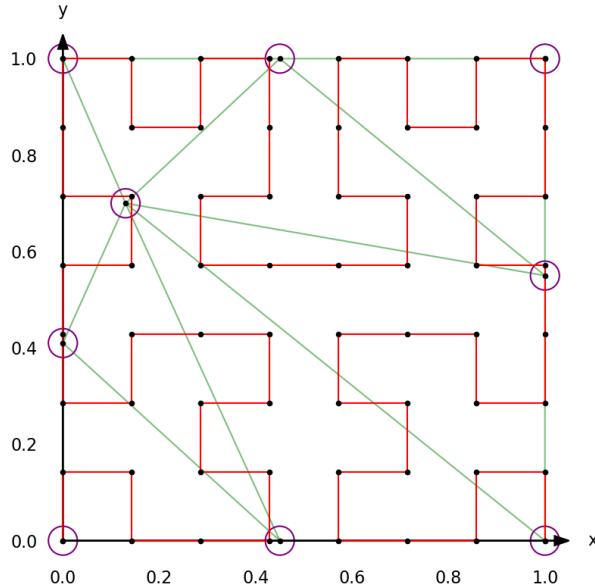


Figure 8: Example of Hilbert points identification for the green-highlighted triangular mesh (the circle radius coincide with τ_{HLB}).

redundancy is finally compressed by means of the Huffman encoding algorithm [28] that assigns short codes to frequent characters and long codes to less recurrent ones and provides a lossless data compression.

The information output of the brightness encoding does coincide with the compressed vectors $\text{DOF}_{HFF}[\tilde{b}_j]$ for each PCA basis \tilde{b}_j , with $j = 1, \dots, k$, namely with the set $\mathcal{D}_{\text{enc}} = \{\text{DOF}_{HFF}[\tilde{b}_j]\}_{j=1}^k$.

3.2.3 The encoding output and validation

The encoding phase delivers the array \mathcal{I}_{enc} and the set \mathcal{D}_{enc} as the necessary information to be stored, together with the averages \overline{ch}_i from (8), values $b_{j,\min}$ and $b_{j,\max}$ from (9), coefficients α_i^j from (13), for $i = 1, \dots, c$, $j = 1, \dots, k$ (see Figure 9 for a sketch). We refer to this information as to the H^2 -PCA-AT (Hilbert and Huffman-encoded PCA-AT) format whose overall storage weight is given by

$$st_{\text{enc}} = \text{bit}_{\mathcal{I}_{\text{enc}}} \cdot nv + \text{bit}_{\mathcal{D}_{\text{enc}}} \cdot \sum_{j=1}^k |\text{DOF}_{HFF}[\tilde{b}_j]| + (c + 2k + ck) \cdot \text{bit}_{PCA}, \quad (15)$$

where $\text{bit}_{\mathcal{I}_{\text{enc}}}$, $\text{bit}_{\mathcal{D}_{\text{enc}}}$ and bit_{PCA} denote the number of bits required to memorize the maximum integer of the list \mathcal{I}_{enc} and of the entries in \mathcal{D}_{enc} , and to store the parameters involved in the PCA. Notice that the last contribution is negligible with respect to the other two terms.

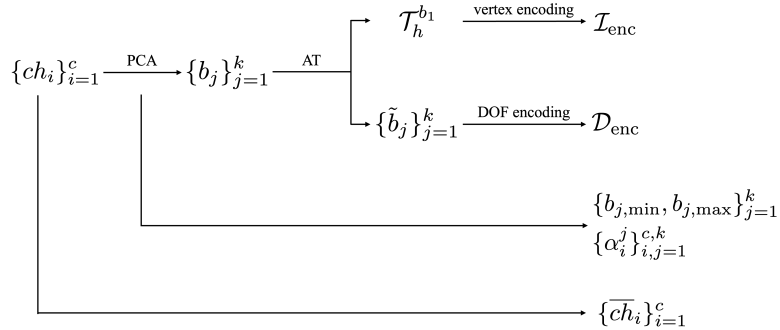


Figure 9: The encoding phase pipeline.

In order to evaluate the effectiveness of the encoding process, we compare this approach with the baseline consisting of directly storing the DOF integers and vertex coordinates floating point numbers without resorting to Hilbert curves and Huffman encoding. A description of the baseline encoding approach follows. Mesh vertices in \mathcal{V} are stored using q digits, such that q is as small as possible and avoids vertex collapse; brightness values are subject to the same procedure as in Section 3.2.2, when skipping the final Huffman encoding.

We carry out such a comparison on the optical observation shown in Figure 5 (left) when an accuracy $\tau = 8.0e-4$ is set for the AT representation of the first basis image b_1 . Table 2 shows the results of this comparison by gathering the number k of the principal components, the file size associated with the H²-PCA-AT format and the baseline encoding, and the storage ratio between the two approaches.

As expected, the weight associated with the two formats increases with the number of principal components. The advantage in using H²-PCA-AT format with respect to the baseline encoding is evident in terms of storage, with an average ratio of 60%.

Table 2: Comparison between the H²-PCA-AT and the baseline format in terms of storage size and ratio.

k	H ² -PCA-AT format [kB]	Baseline encoding [kB]	Storage ratio [%]
1	185320	308952	59.98
3	290560	446264	65.11
5	363856	583576	62.35
7	428253	720888	59.41
11	561402	995512	56.39

3.3 H²-PCA-AT format: the decoding phase

This section is devoted to detail the decoding procedure exploited to recover the information stored via the H²-PCA-AT. We aim to retrieve the mesh together with the associated brightness values. The second task is straightforward when resorting to the Huffman decoding [50] that, starting from \mathcal{D}_{enc} , restores the original redundancy of $\text{DOF}_{HLB-8}[\tilde{b}_j]$, for $j = 1, \dots, k$. At this point, the brightness values in $\text{DOF}_{HLB-8}[\tilde{b}_j]$ are upgraded to the original range $R(b_j)$ in (9), leading to the definition of the new DOF vector $\text{DOF}_{HLB-16}[\tilde{b}_j]$.

Concerning the mesh information, first we transform vector \mathcal{I}_{enc} into the list of the Hilbert indices $\text{ind}_{HLB,\text{sort}}$, by adding the difference between two consecutive Hilbert indices to the previous one. Successively, the vertices in \mathcal{V}_{HLB} of Hilbert points labeled in $\text{ind}_{HLB,\text{sort}}$ are identified, thanks to the one-to-one mapping between Hilbert points and indices. However, vertices do not provide a sufficient information to build a computational mesh, since we have intentionally omitted the encoding of the associated connectivity. Thus, starting from vertices \mathcal{V}_{HLB} , we employ a modified Delaunay algorithm [51] to generate a tessellation of $\bar{\mathcal{Q}}$ that surrogates the original mesh $\mathcal{T}_h^{b_1}$. To this aim, we build a Delaunay grid, $\mathcal{T}_{h,\text{DEL}}^{b_1}$, with vertices $\{V_{HLB,i}\}$. Then, we modify mesh $\mathcal{T}_{h,\text{DEL}}^{b_1}$, which is intrinsically isotropic, into an anisotropic tessellation of $\bar{\mathcal{Q}}$, via the greedy error estimator-based procedure detailed in Algorithm 1.

The input quantities are the Delaunay mesh $\mathcal{T}_{h,\text{DEL}}^{b_1}$ and the vector $\text{DOF}_{HLB-16}[\tilde{b}_1]$. To settle the isotropic-to-anisotropic mesh modification strategy, we first define the FE function $\tilde{b}_{1,\text{DEL}} \in V_h^1(\mathcal{T}_{h,\text{DEL}}^{b_1})$, such that (line 1)

$$\tilde{b}_{1,\text{DEL}}(V_{HLB,i}) = \text{DOF}_{HLB-16}[\tilde{b}_1](i) \quad i = 1, \dots, nv.$$

As a criterion for the mesh modification, we compute the error estimator in (3) applied to function $\tilde{b}_{1,\text{DEL}}$, for each element in $\mathcal{T}_{h,\text{DEL}}^{b_1}$ (line 2). We sort the values of η_K in a descending order and we assemble the list $\mathcal{K}_{\text{sort}}$ of the associated elements K , identified by the triplet of the corresponding vertex labels (line 3). Now, starting from the element K with the highest error estimator, if K does not intersect the boundary $\partial\bar{\mathcal{Q}}$ of the domain (line 4), we identify the three triangles, $\text{Adj}(K)$, adjacent to K . For any $T \in \text{Adj}(K)$, we inspect the two area-equivalent configurations $q_{KT} = \{K, T\}$ and $q_{KT,\text{swap}} = \{K_{\text{swap}}, T_{\text{swap}}\}$, where K_{swap} and T_{swap} are the triangles obtained by swapping the edge common to K and T in the quadrilateral $K \cup T$. This operation is performed under the condition that $K \cup T$ is convex (line 5). The two configurations q_{KT} and $q_{KT,\text{swap}}$ are compared in terms of error estimator, by evaluating $\eta_{KT} = \eta_K + \eta_T$ and $\eta_{KT,\text{swap}} = \eta_{K,\text{swap}} + \eta_{T,\text{swap}}$ (line 6). The algorithm retains the pair of triangles that minimizes such an error estimator (lines 7-8) and consequently updates the

mesh under construction. In particular, we remind that edge swapping may strongly increase the anisotropic features of the grid [52] and this is in line with the anisotropic nature of the original mesh.

Algorithm 1 Isotropic-to-Anisotropic Mesh Recovery Algorithm

Input: $\mathcal{T}_{h,\text{DEL}}^{b_1}$, $\text{DOF}_{HLB-16}[\tilde{b}_1]$

- 1: Project the first PCA basis element on $\mathcal{T}_{h,\text{DEL}}^{b_1}$;
- 2: Evaluate the local error estimator η_K based on $\tilde{b}_{1,\text{DEL}}$, for any $K \in \mathcal{T}_{h,\text{DEL}}^{b_1}$;
- 3: Sort estimators η_K in a descending order and create the list $\mathcal{K}_{\text{sort}}$ of the corresponding elements;
- 4: **for** ($K \in \mathcal{K}_{\text{sort}}$ and $K \cap \partial\mathcal{Q} = \emptyset$) **do**
- 5: **for** ($T \in \text{Adj}(K)$ and q_{KT} convex) **do**
- 6: Compute η_{KT} and $\eta_{KT,\text{swap}}$;
- 7: **if** ($\eta_{KT,\text{swap}} < \eta_{KT}$) **then**
- 8: Replace q_{KT} with $q_{KT,\text{swap}}$;
- 9: **end if**
- 10: **end for**
- 11: **end for**

Output: $\mathcal{T}_{h,\text{rec}}^{b_1}$, $\tilde{b}_{1,\text{rec}}$

The algorithm delivers as final output the new mesh $\mathcal{T}_{h,\text{rec}}^{b_1}$ together with the function $\tilde{b}_{1,\text{rec}} \in V_h^1(\mathcal{T}_{h,\text{rec}}^{b_1})$, such that

$$\tilde{b}_{1,\text{rec}}(V_{\text{HLB},i}) = \text{DOF}_{HLB-16}[\tilde{b}_1](i) \quad i = 1, \dots, nv.$$

Notice that, $\tilde{b}_{1,\text{rec}}$ differs from $\tilde{b}_{1,\text{DEL}}$ due to the different connectivity of meshes $\mathcal{T}_{h,\text{rec}}^{b_1}$ and $\mathcal{T}_{h,\text{DEL}}^{b_1}$, while preserving the brightness values. Also, we observe that the greedy search in line 4 can be limited to a certain percentage of the mesh cardinality for computational saving reasons.

3.3.1 An example of mesh recovery

To investigate the effectiveness of the mesh recovery process, we carry out a comparative analysis in terms of image reconstruction error between an optical observation of reference and the corresponding decoded H²-PCA-AT format based on $\mathcal{T}_h^{b_1}$, on the Delaunay tessellation $\mathcal{T}_{h,\text{DEL}}^{b_1}$, and on the recovered grid $\mathcal{T}_{h,\text{rec}}^{b_1}$.

For comparison purposes, we project the AT representation of \tilde{b}_1 , $\tilde{b}_{1,\text{DEL}}$, and $\tilde{b}_{1,\text{rec}}$ onto the $h \times w$ -px grid characterizing b_1 , by defining the pixelwise quantities

$$B_1(i, j) = \tilde{b}_1(\text{bar}(i, j)), \quad B_{1,\text{DEL}}(i, j) = \tilde{b}_{1,\text{DEL}}(\text{bar}(i, j)), \\ B_{1,\text{rec}}(i, j) = \tilde{b}_{1,\text{rec}}(\text{bar}(i, j)),$$

Table 3: MSE associated with the pixel-wise format B_1 , $B_{1,\text{DEL}}$, $B_{1,\text{rec}}$ for different values of the accuracy τ ; MSE discrepancies; percentage of MSE units gained by the mesh recovery procedure.

τ	1.5e-3	8.0e-4	5.0e-4
$\text{MSE}(b_1, B_1)$	1.049e-3	5.591e-4	3.597e-4
$\text{MSE}(b_1, B_{1,\text{DEL}})$	1.224e-3	6.629e-4	4.307e-4
$\text{MSE}(b_1, B_{1,\text{rec}})$	1.113e-3	5.912e-4	3.827e-4
$\Delta_{1,\text{DEL}-1}$	1.750e-4	1.037e-4	7.108e-5
$\Delta_{1,\text{rec}-1}$	0.6339e-4	3.1990e-5	2.3000e-5
$\%_{\text{recovered}}$	63.74	69.13	67.63

where $\text{bar}(i, j)$ is the barycenter of the pixel (i, j) , for $i = 1, \dots, h$, $j = 1, \dots, w$. This comparison is performed taking as reference the first basis image b_1 in Figure 5. Table 3 gathers the values of: the Mean Squared Error

$$\text{MSE}(b_1, B_*) = \frac{\sum_{i=1}^h \sum_{j=1}^w [b_1(i, j) - B_*(i, j)]^2}{h w}, \quad (16)$$

with $B_* = B_1, B_{1,\text{DEL}}, B_{1,\text{rec}}$, respectively, for three different AT representation accuracy (i.e., values of τ); the discrepancies

$$\Delta_{1,\text{DEL}-1} = \text{MSE}(b_1, B_{1,\text{DEL}}) - \text{MSE}(b_1, B_1),$$

$$\Delta_{1,\text{rec}-1} = \text{MSE}(b_1, B_{1,\text{rec}}) - \text{MSE}(b_1, B_1);$$

the recovered percentage error $\%_{\text{recovered}} = (\Delta_{1,\text{DEL}-1} - \Delta_{1,\text{rec}-1}) / \Delta_{1,\text{DEL}-1} \cdot 100$. These statistics are selected in order to demonstrate that the mesh recovery procedure greatly improves the accuracy of the first basis image approximation based on the mesh $\mathcal{T}_{h, \text{rec}}^{b_1}$ with respect to simply considering the isotropic mesh $\mathcal{T}_{h, \text{DEL}}^{b_1}$.

A comparison of the three pixel-wise formats demonstrates the effectiveness of Algorithm 1. It enhances the MSE linked with $B_{1,\text{DEL}}$, producing an approximation $B_{1,\text{rec}}$ more faithful to the original data b_1 . As AT accuracy improves, both the MSE and related discrepancies decrease. For all the three considered cases, the recovered error percentage remains similar, highlighting the algorithm's consistency in mesh recovery.

3.4 The optical observation reconstruction

The final step consists of reconstructing the original multiband optical observation by resorting to the approximations of the first k basis images b_j and reassembling them through the coefficients α_i^j . To this aim, we first

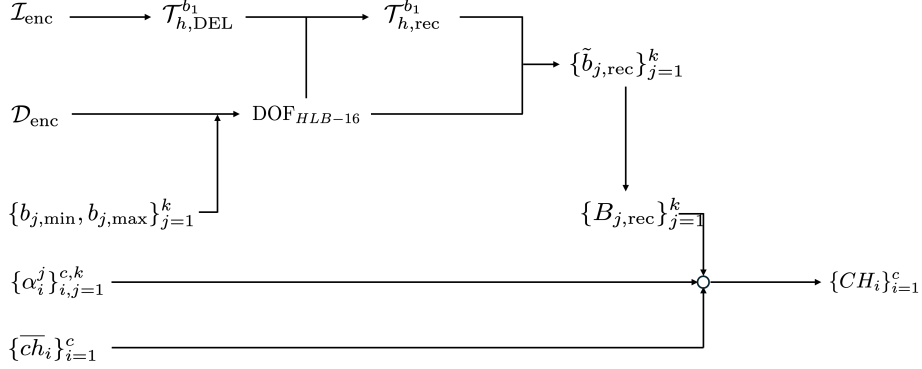


Figure 10: The decoding phase pipeline.

define the finite element functions $\tilde{b}_{j,\text{rec}} \in V_h^1(\mathcal{T}_{h,\text{rec}}^{b_1})$, $j = 1, \dots, k$, such that

$$\tilde{b}_{j,\text{rec}}(V_{\text{HLB},i}) = \text{DOF}_{\text{HLB}-16}[\tilde{b}_j](i) \quad i = 1, \dots, nv,$$

and the corresponding pixel-wise raster representation

$$B_{j,\text{rec}}(p, q) = \tilde{b}_{j,\text{rec}}(\text{bar}(p, q)),$$

with $p = 1, \dots, h$, $q = 1, \dots, w$. Thus, the 3D volume $V_{B,\text{rec}} \in \mathbb{R}^{h \times w \times k}$ associated with the reconstructed matrices $B_{j,\text{rec}}$, the corresponding score matrix U_{rec} and the reconstruction X_{rec} of the sample-feature matrix $X = \mathcal{S}_{\downarrow}(V)$ are given by

$$V_{B,\text{rec}}[:, :, j] = B_{j,\text{rec}} \quad j = 1, \dots, k, \quad U_{\text{rec}} = \mathcal{S}_{\downarrow}(V_{B,\text{rec}}), \quad X_{\text{rec}} = U_{\text{rec}} \Sigma D^T + \bar{X}. \quad (17)$$

Successively, we utilize the PCA expansion in (8) to construct an approximation, CH_i , of the original optical channels ch_i , $i = 1, \dots, c$, computed as

$$ch_i \approx CH_i = \sum_{j=1}^k \alpha_i^j B_{j,\text{rec}} + \overline{ch}_i.$$

In the sequel, we denote by I_{rec} the collection of the reconstructed channels $\{CH_i\}_{i=1}^c$ and by V_{rec} the associated 3D dataset of dimension $h \times w \times c$. The whole pipeline of the decoding is shown in Figure 10.

4 Performance Evaluation

For the performance analysis, we employ two sets of data. The first one is the widely recognized Salinas dataset [53], which comprises hyperspectral images, acquired by the Airborne Visible/Infrared Imaging Spectrometer

(AVIRIS) over Salinas Valley, California, USA. This dataset comprises 204 channels (two of these are shown in Figure 11, first and four columns), each consisting of 512×217 px, spanning the 400 – 2500 nm wavelength range, encompassing visible to near-infrared light. As a second dataset, we con-

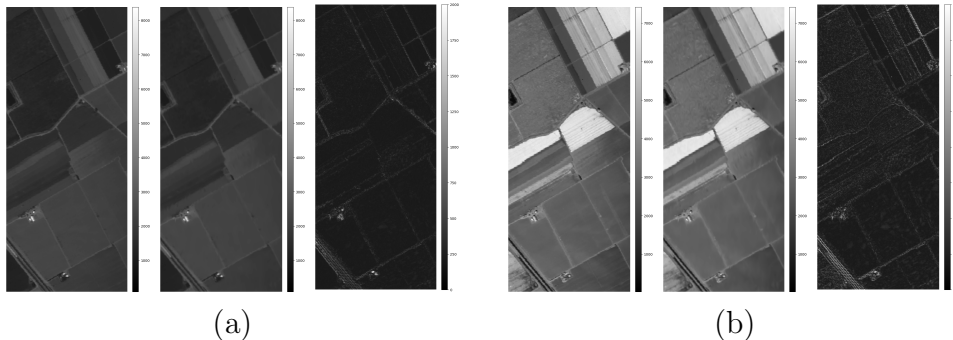


Figure 11: Performance evaluation (reconstruction) on two channels of Salinas dataset, for $i = 10$ (panel (a)) and $i = 40$ (panel (b)): original data ch_i (left), reconstruction CH_i (center) and associated absolute error (right).

sider the optical satellite observation by Sentinel-2 in Figure 5, consisting of 13 channels with 793×1049 px, providing an extremely complex and heterogeneous setting (we show two channels in Figure 12, top row).

We assess the effectiveness of the H^2 -PCA-AT format in terms of image reconstruction, evaluation of a vegetation index, and classification for applications in agriculture and Earth monitoring. In particular, we are interested in investigating the performance characterizing the new format when varying the number k of basis images, the accuracy parameter τ , and when compared with the standard JPEG compression.

4.1 Reconstruction

We first investigate the reconstruction capabilities of the H^2 -PCA-AT format from a qualitative viewpoint over the hyperspectral Salinas dataset in Figure 11 and the Sentinel-2 optical observation in Figure 12. In particular, Figure 11, presents two original Salinas channels (first and fourth columns), the associated H^2 -PCA-AT reconstruction for $k = 10$ and $\tau = 7e-4$ (second and fifth columns), and the corresponding absolute error maps (third and sixth columns). Figure 12 (center row) shows the reconstruction of the Sentinel-2 channels in the top row, for $k = 11$, $\tau = 1.8e-3$. On average, the reconstruction quality is noticeable, especially in the first dataset where the agriculture fields provide easily identifiable features. Such a good quality is confirmed by the maps of the absolute error in both the analyzed cases (third and sixth columns in Figure 11, bottom row in Figure 12).

To quantitatively corroborate these remarks, we refer to a commonly

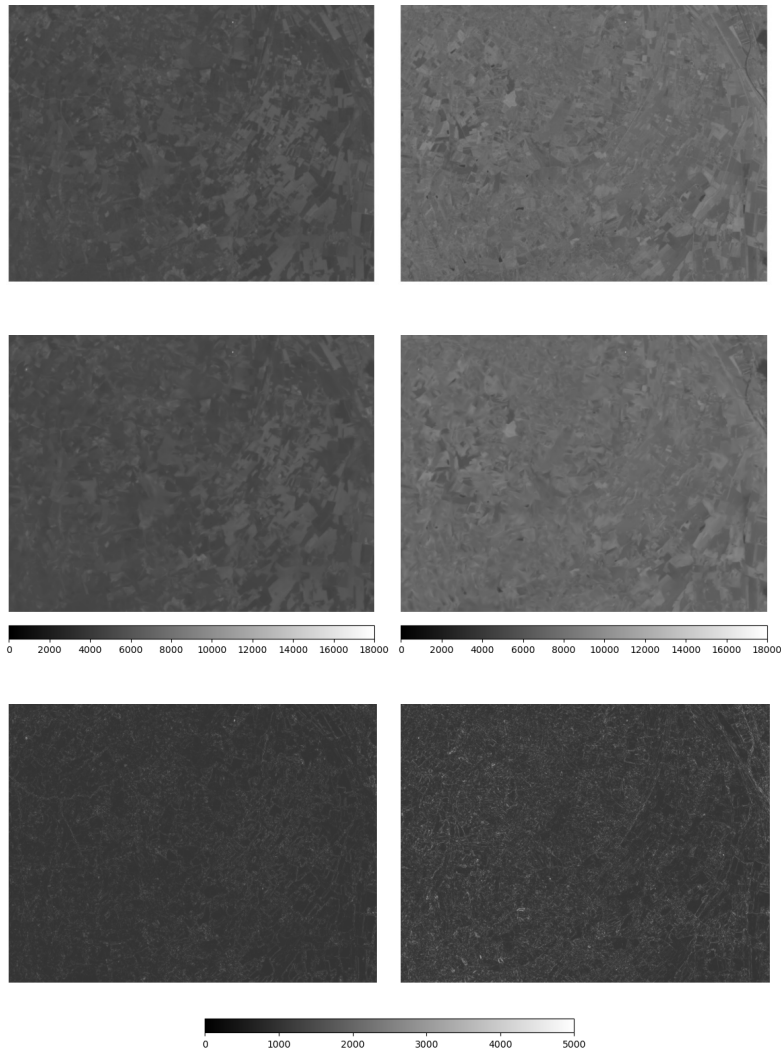


Figure 12: Performance evaluation (reconstruction) on two channels of Sentinel-2 optical observation, for $i = 5$ (left) and $i = 8$ (right): original data ch_i (top), reconstruction CH_i (center) and associated absolute error (bottom).

used performance measure for the lossy compression of an image, namely the Peak Signal-to-Noise Ratio (PSNR). This index quantifies (in decibel) the fidelity of a compressed image, \tilde{I} , with respect to the original data, I , being

$$\text{PSNR}(I, \tilde{I}) = 20 \cdot \log_{10} \left(\frac{\max I}{\sqrt{\text{MSE}(I, \tilde{I})}} \right), \quad (18)$$

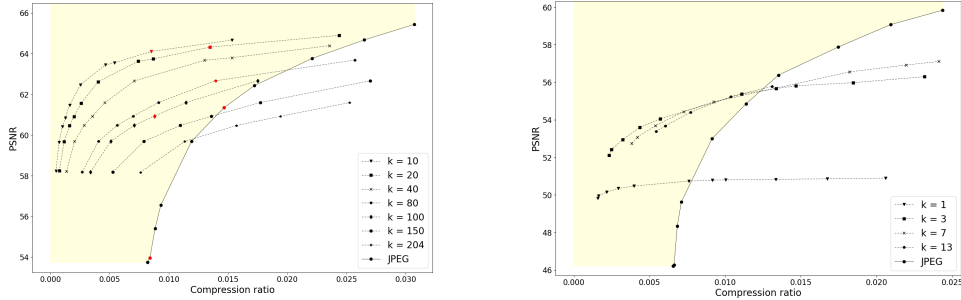


Figure 13: Performance evaluation (reconstruction) for the Salinas (left) and the Sentinel-2 (right) datasets: PSNR_c curves as function of the compression ratio associated with the standard JPEG and the $\text{H}^2\text{-PCA-AT}$ format for different values of k .

where $\max I$ is the maximum brightness value across the image pixels, and MSE is defined as in (16). With reference to the channels in Figures 11-12, we pick $\max I = 2^{16} - 1$, the number of bits required to represent the brightness of each pixel being equal to 16. Moreover, since we deal with multi-channel images, we generalize the definition (18) as

$$\text{PSNR}_c(I_{opt}, I_{rec}) = \frac{1}{c} \sum_{i=1}^c \text{PSNR}(ch_i, CH_i) \quad (19)$$

to include the contribution of all the channels. We investigate the trend of $\text{PSNR}_c(I_{opt}, I_{rec})$ as a function of the compression ratio, namely the ratio between the storage weight in (15) and the size, $st_{opt} = 16 \cdot hwc$, of I_{opt} .

For the $\text{H}^2\text{-PCA-AT}$ format, the compression ratio depends on the number of the PCA basis components as well as on the tolerance τ set for the mesh adaptation, in contrast to a standard JPEG format, which only depends on the quality factor [29]. Figure 13 shows the PSNR_c trend as a function of the compression ratio for the Salinas (left) and the Sentinel-2 (right) optical datasets, by distinguishing different numbers of PCA basis components and different tolerances τ . Table 4 collects the parameters used for the $\text{H}^2\text{-PCA-AT}$ and JPEG formats.

For the Salinas dataset, the maximum PSNR_c value remains comparable ($\simeq 64$) across all choices of k , with larger values of k corresponding to less notable compression ratios. The second dataset leads to a more diversified scenario, since a larger number of PCA components ensures a higher value of the PSNR_c , now ranging from 50 for $k = 1$ to 57 for $k = 7$. As expected, for both the datasets, larger values of τ yield a smaller compression ratio. For comparison, Figure 13 includes the PSNR_c curve of the standard JPEG format, where the compression ratio is adjusted based on the quality factor values in the bottom panel of Table 4. We observe that, for both the datasets, JPEG allows reaching larger values of PSNR_c when moderate com-

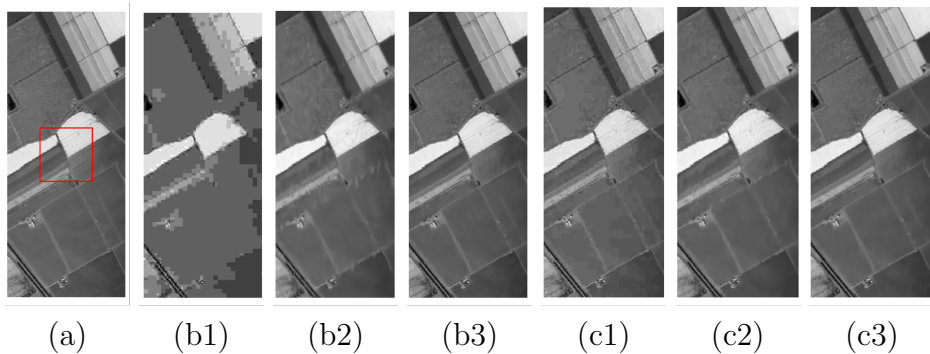


Figure 14: Performance evaluation (reconstruction) on a channel of Salinas dataset, for $i = 40$: original data ch_i (panel (a)); reconstruction for a compression ratio about equal to $8.6e-3$ (panels (b)) and $1.4e-2$ (panels (c)) provided by the JPEG format (panels (b1), (c1)) and by the H²-PCA-AT format (panels (b2), (b3) and (c2), (c3)).

pression ratios are required, exhibiting a 4-unit mismatch with respect to the H²-PCA-AT format. On the contrary, when interested in a small compression ratio, it is advisable to resort to the proposed approach that guarantees high compression while maintaining acceptable $PSNR_c$ values (see Figure 13, where the optimal trade-off between compression ratio and $PSNR_c$ is highlighted in the yellow area).

We have also verified that the standard deviation of the PSNR across channels is similar for both the JPEG and the H²-PCA-AT format, independently of the number k of selected PCA components, the accuracy τ , and the quality factor (≈ 7 for the Salinas, ≈ 10 for the Sentinel-2 observation).

Finally, Figure 14 highlights the two-parameter (k and τ) tunable reconstruction capability of the H²-PCA-AT format, compared to JPEG, which relies on a single parameter (quality factor) to control reconstruction accuracy. Panel (a) shows the original channel ch_{40} of Salinas dataset, while panels (b) and (c) gather the image reconstruction associated with a compression ratio value $\approx 8.6e-3$ and $\approx 1.4e-2$, respectively. Panels (b) and (c) compare the JPEG format with the H²-PCA-AT reconstructions when parameters k and τ are set as in Table 5 (reconstructions (b1)-(b3), (c1)-(c3) correspond to the red markers in the left panel of Figure 13). A qualitative comparison across panels in Figure 14 highlights that the H²-PCA-AT limits the pixel-wise pattern recognizable in the JPEG format, and reduces the presence of artifacts, as confirmed by the enlarged views in Figure 15. From a quantitative perspective, the superiority of the H²-PCA-AT format over standard JPEG is confirmed by the $PSNR_c$ values in Table 5, with a more pronounced percentage quality improvement equal to 15.81% at the smallest compression ratio in panel (b).

Table 4: Performance evaluation (reconstruction): accuracy and quality factor values associated with the different compression ratios in Figure 13.

τ		Quality factor	
Salinas	Sentinel-2	Salinas	Sentinel-2
6.0e-3	3.0e-3	1	1
4.0e-3	2.6e-3	2	2
3.0e-3	2.2e-3	3	3
2.5e-3	1.8e-3	4	4
2.0e-3	1.5e-3	5	5
1.5e-3	9.0e-4	10	10
1.0e-3	8.0e-4	15	15
9.0e-4	7.5e-4	20	20
7.0e-4	7.0e-4	30	30
5.0e-4	6.0e-4	40	40
–	5.0e-4	50	50

Table 5: Performance evaluation (reconstruction): parameter setting used for the comparison in Figure 14.

	Panel	k	τ	Quality factor	Compression ratio	PSNR _c
JPEG	(b1)	–	–	3	8.40e-3	53.9701
H ² -PCA-AT	(b2)	100	2.5e-3	–	8.78e-3	60.9290
H ² -PCA-AT	(b3)	10	7.0e-4	–	8.52e-3	64.1055
JPEG	(c1)	–	–	15	1.46e-2	61.3421
H ² -PCA-AT	(c2)	80	1.5e-3	–	1.39e-2	62.6662
H ² -PCA-AT	(c3)	20	7.0e-4	–	1.35e-2	64.3189

4.2 Normalized Difference Vegetation Index

The Normalized Difference Vegetation Index (NDVI) is a key metric used to assess the presence and health of vegetation on the Earth’s surface. It is derived from multispectral optical imagery, typically captured by satellite sensors or airborne drones equipped with specialized cameras. Its computation is based on the reflectance of light in the near-infrared (NIR) and visible red (Red) bands, according to the formula

$$\text{NDVI} = \frac{\text{NIR} - \text{Red}}{\text{NIR} + \text{Red}}$$

NDVI values range from -1 to $+1$, where values close to $+1$ indicate dense, healthy green vegetation, while negative or near-zero values suggest the absence of vegetation, for instance, in correspondence with water bodies, snow, clouds, urban areas. Indeed, NDVI plays a significant role in agricultural applications (see, e.g.,[54]), where it is used to monitor crop health, providing

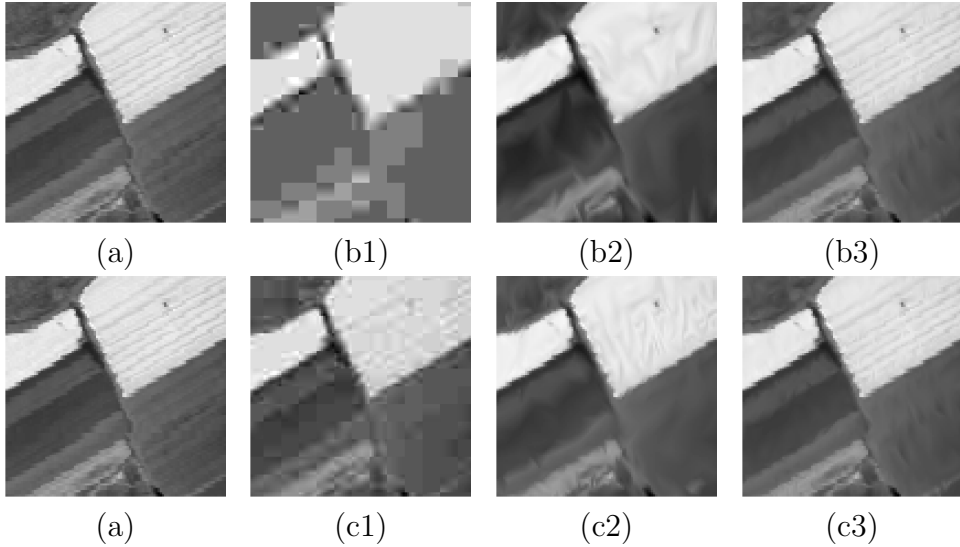


Figure 15: Performance evaluation (reconstruction) on a channel of Salinas dataset, for $i = 40$: enlarged views of panels in Figure 14.

critical information on plant vigour and identifying areas affected by water stress, nutrient deficiency, or disease. Such an index provides useful information in other contexts, such as in forest management to detect deforestation, in environmental science to understand the impact of climate change and human activities on ecosystems, in ecology to study the distribution and dynamics of vegetation.

In this section, we aim to evaluate the performance of H^2 -PCA-AT and JPEG formats in terms of the computation of NDVI map. To this aim, we consider the Sentinel-2 optical dataset in Figure 5. For this dataset, the Red and NIR bands correspond to ch_4 and ch_8 , respectively. As performance measure, we use the PSNR in (18), after setting $\max I$ to the maximum possible NDVI value, i.e., 1. To compare the fidelity of the recovered NDVI distribution, $NDVI_{rec}$, with respect to the original optical NDVI map, $NDVI_{opt}$, in Figure 16, we show the trend of $PSNR(NDVI_{opt}, NDVI_{rec})$ as a function of the compression ratio, for a different number k of principal components and values for the adaptation tolerance τ (see Table 6). We observe that the proposed approach guarantees high compression while maintaining acceptable PSNR values. In particular, the H^2 -PCA-AT format allows for a higher compression when compared with the JPEG, up to quality factor equal to 60.

In Figure 17, we qualitatively compare the JPEG and the H^2 -PCA-AT formats at similar compression ratios (i.e., $6.0e-3$ (high compression), $1.1e-2$ (moderate compression), $1.3e-2$ (low compression)), for the values of k , τ , and for the quality factor in Table 7, corresponding to the red markers in

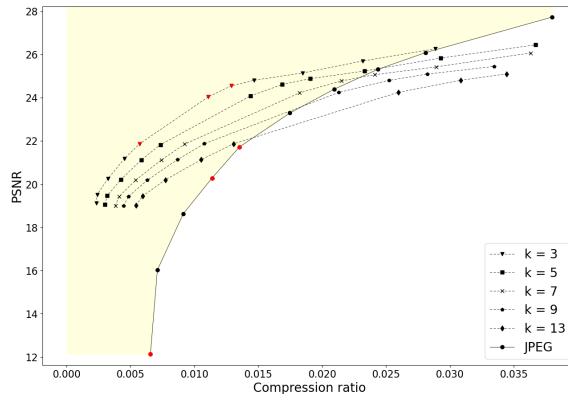


Figure 16: Performance evaluation (NDVI) for the Sentinel-2 dataset: PSNR curves as function of the compression ratio associated with the standard JPEG and the H^2 -PCA-AT format for different values of k .

the figure. The PSNR values in Table 7 confirm the robustness of the H^2 -PCA-AT format, also in the case of the highest compression in panels (b1) and (b2). Indeed, the PSNR mismatch between JPEG and H^2 -PCA-AT increases from 3 to 9 units, when moving towards the highest compression. This feature is corroborated by comparing panels (b1)-(d1) with the corresponding plots in (b2)-(d2).

4.3 Classification task

The H^2 -PCA-AT format has demonstrated to be a reliable tool in reconstructing optical images as well as in the computation of vegetation indices of interest in Environmental Sciences, in particular when dealing with a significant compression. As a last check, we assess the performance of the new format in application prioritizing the preservation of aggregated information instead of the precise pixel values. The extraction of this kind of information pertains several application fields analyzing satellite or aerial imagery, such as environmental monitoring (deforestation[1], desertification[2]), agriculture (land cover[4], crop health[5]) and mineral exploration[3]. In general, such a goal is pursued by using Machine Learning [55] (e.g., Support Vector Machine [56]) or Deep Learning [57, 58] (e.g., Convolutional Neural Networks [59]) algorithms.

In the following, we focus on the land cover classification task [4], which consists of categorizing different types of observed land surface by analyzing the spectral signature of optical images, which reflects differences in vegetation, soil types, water, and man-made materials. As reference database, we adopt the Salinas dataset, since it is widely utilized for classification tasks in precision agriculture. This dataset comprises 204 channels, arranged in the 3D array V , and the ground truth, represented by the 2D array GT .

Table 6: Performance evaluation (NDVI): accuracy and quality factor values associated with the different compression ratios in Figure 16.

τ	Quality factor
3.0e-3	1
2.6e-3	5
2.2e-3	10
1.8e-3	15
1.5e-3	20
9.0e-4	30
8.0e-4	40
7.5e-4	50
7.0e-4	60
6.0e-4	75
5.0e-4	-

Table 7: Performance evaluation (NDVI): parameter setting used for the comparison in Figure 17.

	Panel	k	τ	Quality factor	Compression ratio	PSNR
JPEG	(b1)	-	-	1	6.55e-3	12.1263
H ² -PCA-AT	(b2)	3	1.5e-3	-	5.70e-3	21.8584
JPEG	(c1)	-	-	15	1.13e-2	20.2771
H ² -PCA-AT	(c2)	3	9.0e-4	-	1.10e-2	24.0368
JPEG	(d1)	-	-	20	1.35e-2	21.7125
H ² -PCA-AT	(d2)	3	8.0e-4	-	1.29e-2	24.5459

In particular, GT contains the land cover labels associated with 16 labeled classes, including broccoli weeds, fallow, stubble, and lettuce, as depicted by Figure 18, left panel.

We use a classification model built on the supervised learning algorithm Support Vector Machine (SVM). This algorithm identifies the decision boundary, which is a hyperplane or curve in the feature space designed to separate classes by maximizing the margin, or the distance between the boundary and the nearest data points of each class. These critical points, called support vectors, determine the boundary’s position and orientation, ensuring effective separation even in challenging or high-dimensional datasets. To handle cases where the data is not linearly separable, the SVM uses the kernel trick, which maps the data into a higher-dimensional space where it becomes easier to classify. Specifically, we select the Radial Basis Function (RBF) kernel[60] for this purpose.

To evaluate the performance of the H²-PCA-AT format in land cover classification, we apply a training-test split to the dataset V . In this regard,

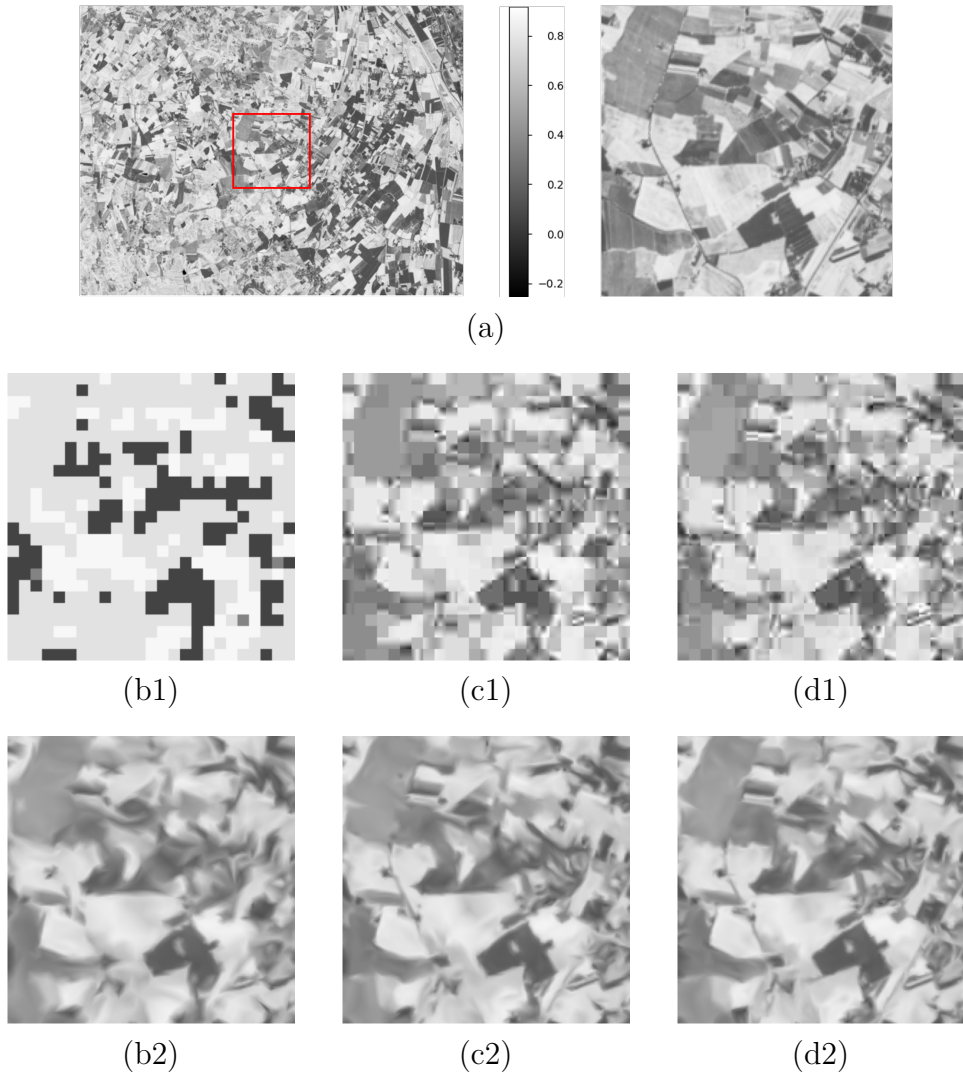


Figure 17: Performance evaluation (NDVI) on the Sentinel-2 dataset: original data and enlarged view (panel (a)); reconstruction for a compression ratio about equal to $6.0e-3$ (panels (b)), $1.1e-2$ (panels (c)) and $1.3e-2$ (panels (d)) provided by the JPEG format (panels (b1), (c1), (d1)) and by the H^2 -PCA-AT format (panels (b2), (c2), (d2)).

we cannot resort to the standard random split of the image pixels since the AT representation works on the whole image (or on an associated rectangular portion). Thus, we split the array V into two subsets, the left, V_1 , and the right, V_2 , half. Figure 18, center panel, shows the corresponding 2-dimensional ground truth subsets, GT_1 and GT_2 . Furthermore, since some land cover classes might be present only in one half, we focus on pixels belonging to classes common to both halves. Pixels not meeting this con-

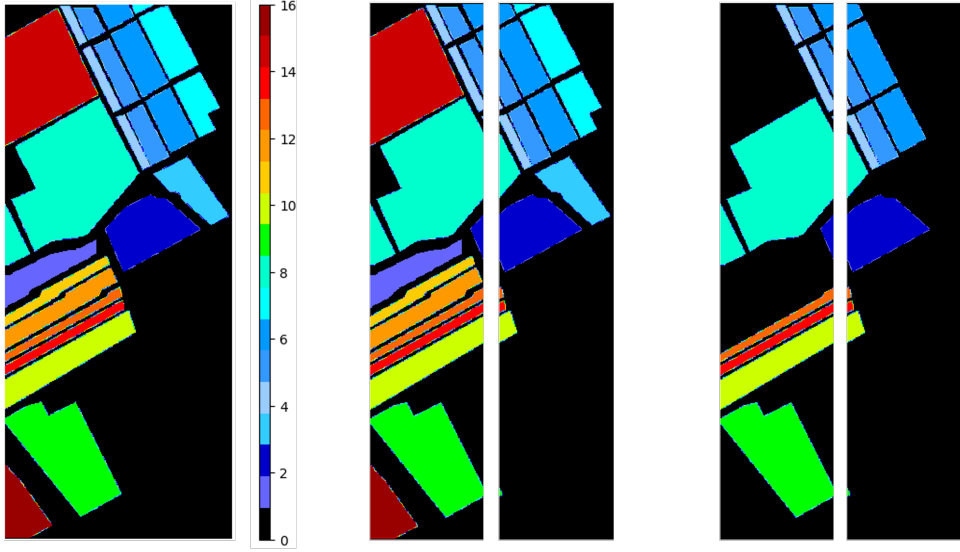


Figure 18: Performance evaluation (classification) for the Salinas dataset: ground truth GT (left panel); splitting of the data into two portions before (center panel) and after (right panel) the post-processing.

dition are post-processed and assigned to the background class, thus being excluded from the training process (see Figure 18, right). Table 8 categorizes the 16 labeled classes together with the background in terms of pixel count associated with GT, by distinguishing among the whole array, the label subsets corresponding to V_1 and V_2 for the original (GT_1 and GT_2) and for the post-processed ($GT_{1,new}$ and $GT_{2,new}$) data.

In practice, we adopt the K -fold cross-validation method [61]. We define the 2D sample-feature matrices $X_1 = \mathcal{S}_\downarrow(V_1)$ and $X_2 = \mathcal{S}_\downarrow(V_2)$, and the associated 1D ground truth vectors, $Y_1 = s_\downarrow(GT_{1,new})$ and $Y_2 = s_\downarrow(GT_{2,new})$, with $s_\downarrow : \mathbb{R}^{h \times w} \rightarrow \mathbb{R}^{hw}$, and

$$Y_i[(r-1)w + q] = GT_{i,new}[r, q] \quad r = 1, \dots, h, \quad q = 1, \dots, w, \quad i = 1, 2.$$

The 2 folds $\{X_1, Y_1\}$ and $\{X_2, Y_2\}$ are alternatively used to define the training, $\{X_{trn}, Y_{trn}\}$, and the testing, $\{X_{tst}, Y_{tst}\}$, sets. In particular, we select the K -th fold as

$$\begin{cases} \{X_{trn}, Y_{trn}\} = \{X_1, Y_1\}, & \{X_{tst}, Y_{tst}\} = \{X_{2,rec}, Y_2\} & \text{for } K = 1, \\ \{X_{trn}, Y_{trn}\} = \{X_2, Y_2\}, & \{X_{tst}, Y_{tst}\} = \{X_{1,rec}, Y_1\} & \text{for } K = 2, \end{cases} \quad (20)$$

where $X_{i,rec}$ is the sample-feature matrix associated with the H^2 -PCA-AT format of V_i , according to (17), for $i = 1, 2$. The testing phase on the single fold evaluates the model performance in terms of the accuracy score, i.e., the number of correct classifications divided by the overall predictions. Concerning the effectiveness of the whole model, it is quantified by averaging

Table 8: Pixel count for the 16 labeled classes and for the background in GT and the split portions, before and after the post-processing.

Class	Label	GT	GT ₁	GT ₂	GT _{1,new}	GT _{2,new}
0	Background	56975	16887	40088	30966	45643
1	Broccoli green, weeds 1	2009	2009	0	0	0
2	Broccoli green, weeds 2	3726	272	3454	272	3454
3	Fallow	1976	0	1976	0	0
4	Fallow-rough plow	1394	905	489	905	489
5	Fallow smooth	2678	1110	1568	1110	1568
6	Stubble	3959	389	3570	389	3570
7	Celery	3579	0	3579	0	0
8	Grapes-untrained	11271	10636	635	10636	635
9	Soil-vineyard development	6203	6187	16	6187	16
10	Corn-senesced green weeds	3278	2931	347	2931	347
11	Lettuce-romaine, 4 weeks	1068	1068	0	0	0
12	Lettuce-romaine, 5 weeks	1927	1927	0	0	0
13	Lettuce-romaine, 6 weeks	916	883	33	883	33
14	Lettuce-romaine, 7 weeks	1070	1017	53	1017	53
15	Vineyard-untrained	7268	7268	0	0	0
16	Vineyard-vertical trellis	1807	1807	0	0	0

the accuracy scores across the two folds.

For comparison purpose, we apply the SVM algorithm to the JPEG format, by exploiting the same training and testing splitting strategy and by selecting the K -th fold as in (20), after replacing $X_{i,rec}$ with the corresponding JPEG reconstruction, for $i = 1, 2$. Figure 19 shows the results of this comparison in terms of classification accuracy as a function of the compression ratio, for different values of k and τ for the H²-PCA-AT format, and of the quality factor when considering the standard JPEG (we refer to Table 9 and Figure 19 for all the details). Consistently with Figures 13 and 16, we observe that the H²-PCA-AT format outperforms JPEG when dealing with low compression ratio, without compromising the classification performance. Table 10 and Figure 20 highlight this behavior from a quantitative and qualitative viewpoint, respectively by comparing the output of the H²-PCA-AT and the JPEG formats for a similar accuracy. The new format ensures the same classification quality while achieving 16 times more compression than JPEG.

5 Conclusions and Perspectives

This paper introduces a novel compression framework for multiband optical satellite imagery, addressing critical challenges in storage and transmission, with a particular focus on agriculture. The proposed approach integrates

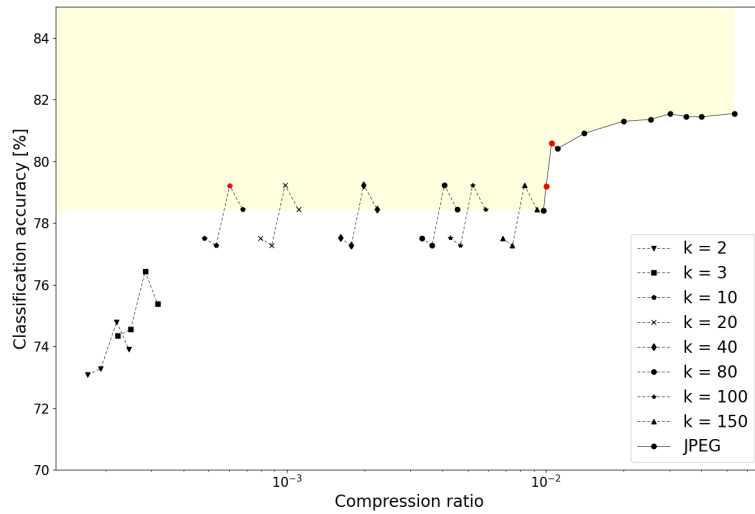


Figure 19: Performance evaluation (classification) for the Salinas dataset: classification accuracy curves as function of the compression ratio associated with the standard JPEG and the H²-PCA-AT format for different values of k .

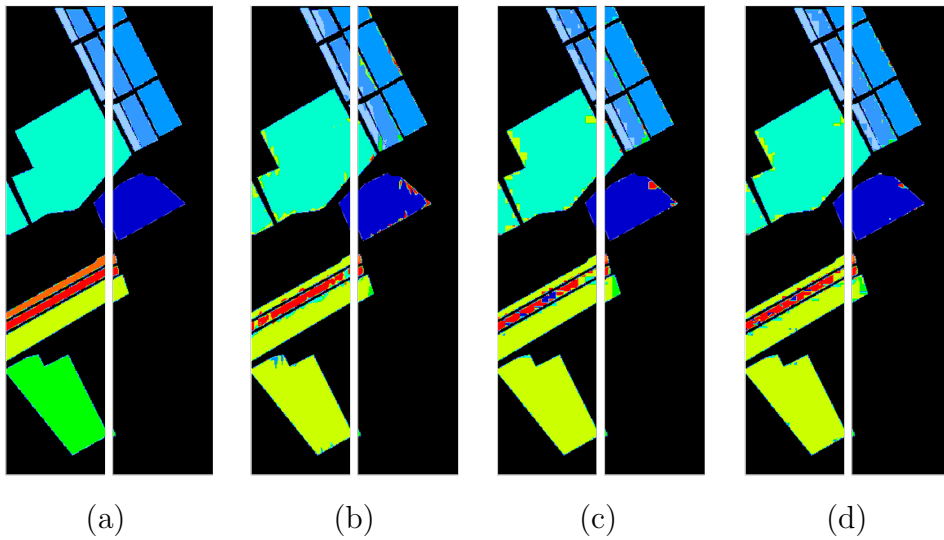


Figure 20: Performance evaluation (classification) for the Salinas dataset: post-processed ground truth (panel (a)); classification for a similar accuracy provided by the H²-PCA-AT format (panel (b)) and by the JPEG format (panels (c), (d)).

PCA (Principal Component Analysis) with anisotropic mesh adaptation to create the PCA-AT (PCA-Adaptive Triangular) representation. Success-

Table 9: Performance evaluation (classification): accuracy and quality factor values associated with the different compression ratios in Figure 19.

τ	Quality factor
1.0e-2	1
9.0e-3	2
8.0e-3	3
7.0e-3	4
–	5
–	10
–	15
–	20
–	30
–	40
–	50
–	60
–	75

Table 10: Performance evaluation (classification): parameter setting used for the comparison in Figure 20.

	Panel	k	τ	Quality factor	Compression ratio	Classification accuracy
H ² -PCA-AT	(b)	10	8.0e-3	–	6.02e-4	79.2182
JPEG	(c)	–	–	3	1.00e-2	79.1915
JPEG	(d)	–	–	4	1.05e-2	80.5851

sively, Hilbert space-filling curves with Huffman encoding are applied to this representation to optimize storage, eliminating mesh connectivity information. This stage leads to the H²-PCA-AT format. Finally, to ensure a reliable restoration of the compressed data, we settle a decoding phase with a particular care to recover the mesh data. To this aim, we propose a Delaunay-based algorithm, which exploits an a posteriori error analysis, properly customized to the anisotropic setting. The framework is validated across agriculture applications such as full data reconstruction, NDVI (Normalized Difference Vegetation Index) computation, land cover classification.

The method offers clear advantages. By replacing uniform pixel grids with adaptive triangular meshes, it achieves high compression with respect to traditional methods like JPEG, without compromising data fidelity. In addition, the possibility to tune parameters k and τ allows the customization of the H²-PCA-AT format to specific application needs, ensuring different compression efficiency-to-quality scenarios. Despite its advantages, the H²-PCA-AT format has certain limitations. The lossy nature of the compression introduces small inaccuracies that may not be acceptable when precise quantitative analysis is required. However, for qualitative and semi-

quantitative applications like those prevalent in agriculture, the trade-off between compression ratio and accuracy is well justified.

Future research will focus on automating the selection of PCA components and mesh adaptation tolerances to eliminate manual tuning. Additionally, exploring alternative mesh metrics and metric intersection algorithms could enhance the AT representation by capturing diverse image features. Finally, leveraging the graph-like structure of the H^2 -PCA-AT format in Graph Convolutional Networks (GCNs) [62] holds promise for efficient and accurate classification, reducing computational costs and resource demands.

Author contributions

Luca Liverotti: conceptualization, methodology, software, validation, investigation, data curation, writing – original draft preparation, visualization. **Nicola Ferro:** conceptualization, methodology, software, validation, investigation, writing – original draft preparation. **Matteo Matteucci:** conceptualization, methodology, software, validation, investigation, writing – review and editing, supervision, project administration. **Simona Perotto:** conceptualization, methodology, software, validation, investigation, writing – original draft preparation, supervision, project administration.

Acknowledgments

LL, NF and SP acknowledge the support by MUR, grant Dipartimento di Eccellenza 2023–2027. LL, NF and SP are members of the Gruppo Nazionale Calcolo Scientifico–Istituto Nazionale di Alta Matematica (GNCS–INdAM). NF acknowledges the INdAM–GNCS 2024 Project “Accuratezza geometrica e adattività di griglia per problemi con interfacce complesse”. MM acknowledges the support of Agritech National Research Center and received funding from the European Union Next-GenerationEU (PIANO NAZIONALE DI RIPRESA E RESILIENZA (PNRR) – MISSIONE 4 COMPONENTE 2, INVESTIMENTO 1.4 – D.D. 1032 17/06/2022, CN00000022).

Data Availability Statement

The data that support the findings of this study are available at <https://scihub.copernicus.eu/> and https://www.ehu.eus/ccwintco/index.php/Hyperspectral_Remote_Sensing_Scenes.

References

- [1] Lee SH, Han KJ. Classification of landscape affected by deforestation using high-resolution remote sensing data and deep-learning techniques. *Remote Sensing*. 2020;12:3372.
- [2] Jarocińska A, Kopeć D, Niedzielko J. The utility of airborne hyperspectral and satellite multispectral images in identifying Natura 2000 non-forest habitats for conservation purposes. *Scientific Reports*. 2023;13:4549.
- [3] van der Meer FD, van der Werff HMA. Multi- and hyperspectral geologic remote sensing: a review. *International Journal of Applied Earth Observation and Geoinformation*. 2012;14:112-128.
- [4] Vali A, Comai S, Matteucci M. Deep learning for land use and land cover classification based on hyperspectral and multispectral Earth observation data: a review. *Remote Sensing*. 2020;12:2495.
- [5] Thenkabail PS, Lyon JG. *Hyperspectral Remote Sensing of Vegetation*. CRC Press, 2011.
- [6] Wulder MA, Roy DP. Fifty years of Landsat science and impacts. *Remote Sensing of Environment*. 2022;280:113195.
- [7] Seshadri KSV, Rao M. Resourcesat-1: a global multi-observation mission for resources monitoring. *Acta Astronautica*. 2005;57:534-539.
- [8] Chen L, Letu H. An introduction to the chinese high-resolution Earth observation system: Gaofen-1 7 civilian satellites. *Journal of Remote Sensing*. 2022;3:1-14.
- [9] Jutz S, Milagro-Perez MP. Copernicus: the European Earth Observation programme. *Revista de TELEDETECCION*. 2020;56:V-XI.
- [10] Campbell BA. *Radar Remote Sensing of Planetary Surfaces*. Cambridge University Press, 2002.
- [11] Qian S. *Optical Satellite Signal Processing and Enhancement*. SPIE, 2013.
- [12] Lillesand T, Kiefer RW, Chipman JW. *Remote Sensing and Image Interpretation*. Wiley, 2015.
- [13] Manolakis DG, Lockwood RB, Cooley TW. *Hyperspectral Imaging Remote Sensing*. Cambridge University Press, 2016.

- [14] Bascónes D, González C, Mozos D. FPGA implementation of the CCSDS 1.2.3 standard for real-time hyperspectral lossless compression. *IEEE Journal of Selected Topics in Applied Earth Observations and Remote Sensing*. 2017;PP:1-8.
- [15] Bascónes D, González C, Mozos D. Parallel implementation of the CCSDS 1.2.3 standard for hyperspectral lossless compression. *Remote Sensing*. 2017;9:973.
- [16] Motta G, Rizzo F, Storer J. *Hyperspectral Data Compression*. Springer Science & Business Media, 2006.
- [17] Jolliffe IT. *Principal Components Analysis*. Springer, 2002.
- [18] Du Q, Fowler JE. Hyperspectral image compression using JPEG2000 and Principal Component Analysis. *IEEE Geoscience and Remote Sensing Letters*. 2007;4(2):201–205.
- [19] Bascónes D, González C, Mozos D. Hyperspectral image compression using vector quantization, PCA and JPEG2000. *Remote Sensing*. 2018;10:907.
- [20] Zhu W, Du Q, Fowler JE. Segmented PCA and JPEG2000 for hyperspectral image compression. *Proceedings of SPIE - The International Society for Optical Engineering*. 2009;7455.
- [21] Du Q, Ly N, Fowler JE. An operational approach to PCA+JPEG2000 compression of hyperspectral imagery. *IEEE Journal of Selected Topics in Applied Earth Observations and Remote Sensing*. 2014;7(6):2237-2245.
- [22] Sanjith S, Ganesan R. A review on hyperspectral image compression. *2014 International Conference on Control, Instrumentation, Communication and Computational Technologies (ICCICCT)*. 2014:1159-1163.
- [23] Formaggia L, Perotto S. New anisotropic a priori estimates. *Numerische Mathematik*. 2001;89:641-667.
- [24] Micheletti S, Perotto S. Anisotropic adaptation via a Zienkiewicz-Zhu error estimator for 2D elliptic problems. *Numerical Mathematics and Advanced Applications*. 2010:645-653.
- [25] Lelechenko L. IoT in Agriculture: Paving the Way for Smart Farming. <https://www.ietfforall.com>; 2024. Accessed: September 26, 2024.
- [26] Astrocast . How Satellite IoT takes farming to the next level. <https://www.astrocast.com>; 2023. Accessed: September 26, 2024.

- [27] Hilbert D. Ueber die stetige Abbildung einer Line auf ein Flächenstück. *Mathematische Annalen*. 1891;38:459-460.
- [28] Huffman D. A method for the construction of minimum-redundancy codes. *Proceedings of the IRE*. 1952;40:1098-1101.
- [29] Wallace GK. The JPEG still picture compression standard. *IEEE Transactions on Consumer Electronics*. 1992;38:18-34.
- [30] Bineeth K, Preena KP. A review on 2D image representation methods. *International Journal of Engineering Research and Technology*. 2015;4:1075 - 1081.
- [31] Shusterman E, Feder M. Image compression via improved quadtree decomposition algorithms. *IEEE Transactions on Image Processing*. 1994;3:207-215.
- [32] Chiappa A, Micheletti S, Peli R, Perotto S. Mesh adaptation-aided image segmentation. *Communications in Nonlinear Science and Numerical Simulation*. 2019;74:147-166.
- [33] Giacomini M, Perotto S. Anisotropic mesh adaptation for region-based segmentation accounting for image spatial information. *Computers & Mathematics with Applications*. 2022;121:1–17.
- [34] Ern A, Guermond JL. *Theory and Practice of Finite Elements*. Volume 159 of *Applied Mathematical Sciences*. Springer-Verlag, 2004.
- [35] Ainsworth M, Oden JT. *A Posteriori Error Estimation in Finite Element Analysis*. John Wiley & Sons, 2000.
- [36] Bangerth W, Rannacher R. *Adaptive Finite Element Methods for Differential Equations*. Birkhäuser Verlag, 2003.
- [37] Verfürth R. *A Review of A Posteriori Error Estimation and Adaptive Mesh-Refinement Technique*. Wiley-Teubner, 1996.
- [38] Zienkiewicz OC, Zhu JZ. A simple error estimator and adaptive procedure for practical engineering analysis. *International Journal for Numerical Methods in Engineering*. 1987;24(2):337–357.
- [39] Zienkiewicz OC, Zhu JZ. The superconvergent patch recovery and a posteriori error estimates. I. The recovery technique. *International Journal for Numerical Methods in Engineering*. 1992;33(7):1331–1364.
- [40] Zienkiewicz OC, Zhu JZ. The superconvergent patch recovery and a posteriori error estimates. II. Error estimates and adaptivity. *International Journal for Numerical Methods in Engineering*. 1992;33(7):1365–1382.

- [41] Frey PJ, George PL. *Mesh Generation. Application to Finite Elements*. John Wiley & Sons. second ed., 2008.
- [42] Micheletti S, Perotto S. Reliability and efficiency of an anisotropic Zienkiewicz-Zhu error estimator. *Computer Methods in Applied Mechanics and Engineering*. 2006;195(9-12):799–835.
- [43] Hecht F. New development in FreeFem++. *Journal of Numerical Mathematics*. 2012;20(3-4):251–265.
- [44] Hastie T, Tibshirani R, Friedman J. *The Elements of Statistical Learning*. Springer, 2009.
- [45] Bader M. *Space-Filling Curves: an Introduction with Applications in Scientific Computing*. Springer, 2013.
- [46] Lawder J, King P. Using space-filling curves for multi-dimensional indexing. *Advances in Databases*. 2000;1832:20-35.
- [47] Peano G. Sur une courbe, qui remplit toute une aire plane. *Mathematische Annalen*. 1890;160:36-157.
- [48] Morton GM. *A Computer Oriented Geodetic Data Base and a New Technique in File Sequencing*. IBM Ltd., 1966.
- [49] Hilbert curve Python package. <https://pypi.org/project/hilbertcurve/>.
- [50] Huffman encoding Python package. <https://github.com/bhrigu123/huffman-coding>.
- [51] Berg M, Cheong O, Kreveld M, Overmars M. *Computational Geometry: Algorithms and Applications*. Springer, 2008.
- [52] Borouchaki H, Laug P, George PL. Parametric surface meshing using a combined advancing-front generalized Delaunay approach. *International Journal for Numerical Methods in Engineering*. 2000;49(1–2):233–259.
- [53] Indian Pines dataset. https://www.ehu.eus/ccwintco/index.php/Hyperspectral_Remote_Sensing_Scenes.
- [54] Pettorelli N. *The Normalized Difference Vegetation Index*. Oxford University Press, 2013.
- [55] Mohri M, Rostamizadeh A, Talwalkar A. *Foundations of Machine Learning*. MIT Press, 2012.

- [56] Cristianini N, Shawe-Taylor J. *An Introduction to Support Vector Machines and Other Kernel-based Learning Methods*. Cambridge University Press, 2000.
- [57] Chollet F. *Deep Learning with Python*. Manning Publications, 2017.
- [58] Poonia RC, Nayak SR, Singh V. *Deep Learning for Sustainable Agriculture*. Academic Press, 2022.
- [59] Venkatesan R, Li B. *Convolutional Neural Networks in Visual Computing*. CRC Press, 2017.
- [60] Patle A, Chouhan DS. SVM kernel functions for classification. *International Conference on Advances in Technology and Engineering*. 2013:1-9.
- [61] Stone M. Cross-validatory choice and assessment of statistical predictions. *Journal of the Royal Statistical Society*. 1974;36:111-133.
- [62] Zhang S, Tong H, Xu J. Graph convolutional networks: a comprehensive review. *Computational Social Networks*. 2019;6:11.

MOX Technical Reports, last issues

Dipartimento di Matematica
Politecnico di Milano, Via Bonardi 9 - 20133 Milano (Italy)

- 108/2024** Arostica, R.; Nolte, D.; Brown, A.; Gebauer, A.; Karabelas, E.; Jilberto, J.; Salvador, M.; Bucelli, M.; Piersanti, R.; Osouli, K.; Augustin, C.; Finsberg, H.; Shi, L.; Hirschvogel, M.; Pfaller, M.; Africa, P.C.; Gsell, M.; Marsden, A.; Nordsletten, D.; Regazzoni, F.; Plank, G.; Sundnes, J.; Dede', L.; Peirlinck, M.; Vedula, V.; Wall, W.; Bertoglio, C.
A software benchmark for cardiac elastodynamics
- 107/2024** Chen, J.; Ballini, E.; Micheletti, S.
Active Flow Control for Bluff Body under High Reynolds Number Turbulent Flow Conditions Using Deep Reinforcement Learning
- 106/2024** Brunati, S.; Bucelli, M.; Piersanti, R.; Dede', L.; Vergara, C.
Coupled Eikonal problems to model cardiac reentries in Purkinje network and myocardium
- 105/2024** Bartsch, J.; Barakat, A.A.; Buchwald, S.; Ciaramella, G.; Volkwein, S.; Weig, E.M.
Reconstructing the system coefficients for coupled harmonic oscillators
- 104/2024** Cerrone, D.; Riccobelli, D.; Vitullo, P.; Ballarin, F.; Falco, J.; Acerbi, F.; Manzoni, A.; Zunino, P.; Ciarletta, P.
Patient-specific prediction of glioblastoma growth via reduced order modeling and neural networks
- 103/2024** Fois, M.; Gatti, F.; de Falco, C.; Formaggia, L.
A comparative analysis of mesh-based and particle-based numerical methods for landslide run-out simulations
- 101/2024** Bonetti, S.; Corti, M.
Unified discontinuous Galerkin analysis of a thermo/poro-viscoelasticity model
- 102/2024** Bucelli, M.
The lifex library version 2.0
- 100/2024** Farenga, N.; Fresca, S.; Brivio, S.; Manzoni, A.
On latent dynamics learning in nonlinear reduced order modeling
- 99/2024** Ragni, A.; Masci, C.; Paganoni, A. M.
Analysis of Higher Education Dropouts Dynamics through Multilevel Functional Decomposition of Recurrent Events in Counting Processes